45th AIAA Aerospace Sciences Meeting and Exhibit
8 - 11 January 2007, Reno, Nevada

AIAA 2007-946

Numerical Simulation of Hypersonic Boundary-Layer Receptivity to Two and Three-dimensional Wall Perturbations

Xiaowen Wang * **and Xiaolin Zhong** †
Mechanical and Aerospace Engineering Department
University of California, Los Angeles, California 90095

Abstract

The receptivity of a Mach 5.92 flow over a flat plate to two and three-dimensional wall perturbations is investigated in this paper by numerical simulations and linear stability theory (LST). The 2D steady base flow is simulated by solving two-dimensional compressible Navier-Stokes equations with a combination of a fifth-order shock-fitting finite difference method and a second-order TVD scheme. Three-dimensional steady base flow is extended from 2D base flow due to the fact that the flow field on a flat plate is independent of spanwise coordinate. The characteristics of boundary-layer wave modes are identified and evaluated by comparing the results of LST and numerical simulations. Two-dimensional wall perturbations of six cases are introduced to 2D steady base flow by a forcing slot located on the flat plate. The numerical results show that all six cases of 2D wall perturbations eventually result in the same type of instability wave (mode S) in the boundary layer, which indicates that receptivity of the hypersonic boundary layer to 2D wall perturbations is independent of the specific type and profile of perturbations. It is also found that the hypersonic boundary-layer flow is more sensitive to blowing-suction than to wall oscillation and temperature perturbations, which is consistent with the theoretical and numerical analysis of Fedorov and Khokhlov [1]. The receptivity of the hypersonic boundary layer to temperature perturbation is proportional to the energy introduced to the steady base flow. In order to investigate the transient growth phenomena, small-scale stationary three-dimensional roughness elements are introduced on the flat plate. The surface roughness is periodic in spanwise direction. Effect of thermal flat plate boundary conditions on the receptivity process is considered by comparing numerical simulations on adiabatic and isothermal flat plates, respectively. The numerical results show that counter rotating streamwise vortices are excited by stationary roughness element. The temperature increases in the wake region of convex surface roughness whereas it decreases in the wake region of concave surface roughness. Furthermore, the speed of wake from convex surface roughness is slower than that from concave roughness. All these results are consistent with those of Tumin's theoretical analysis [2]. It is also concluded based on the numerical results that the roughness element on adiabatic flat plate is more efficient in the excitations of streamwise vortices and transient growth.

1 Introduction

Due to the fact that a turbulent flow generates much higher shear stress and heat flux to the wall than a laminar flow, the performance and control of hypersonic vehicles are significantly affected by the laminar-turbulent transition of the boundary-layer flows over vehicle surfaces. So the accurate prediction of boundary-layer transition location is very important to the drag calculation and aerothermal design of hypersonic vehicles.

In order to predict and control boundary-layer transition, extensive studies have been carried out to reveal transition mechanisms. It is found that the transition mechanism of a boundary-layer flow depends on the amplitude level of environment disturbances. In an environment of small amplitude disturbances, the transition of the boundary-layer flow over a smooth surface generally consists of the following three stages:

- Stage 1: Receptivity process during which small amplitude environmental disturbances enter the boundary layer and excite boundary-layer wave modes;

*Graduate Student Researcher,Mechanical and Aerospace Engineering Department, Member AIAA
†Professor, Mechanical and Aerospace Engineering Department,Associate Fellow AIAA.

- Stage 2: Linear development or growth of unstable boundary-layer wave modes which can be obtained by solving the eigen-problem of the homogeneous linearized stability equations;
- Stage 3: Boundary-layer transition from laminar to turbulent caused by non-linear and three-dimensional effects when the unstable wave modes reach certain amplitudes.

For high amplitude disturbances, laminar boundary-layer flow can transit to turbulence right after the receptivity process due to strong initial excitations of boundary-layer modes. Over nonsmooth surface with roughness elements, the transient growth of boundary-layer waves may directly lead to transition. All these transitions relating to high amplitude disturbances and transient growth are called bypass transition.

According to the transition mechanisms, it is clearly demonstrated that the study of receptivity process is important because it provides initial conditions of amplitude, frequency, and phase angle for boundary-layer wave modes [3]. Furthermore, the receptivity process of supersonic and hypersonic boundary-layer flows is more complex than that of subsonic or incompressible flows due to the additional effects of shock wave, compressibility, high temperature, etc. It has motivated extensive theoretical, experimental, and numerical studies on the excitations of boundary-layer wave modes in two-dimensional and three-dimensional high speed boundary layers.

In 1975, Mack [4] used the compressible LST to calculate the amplitude ratio of constant-frequency disturbances for insulated and cooled-wall flat-plate supersonic boundary layers. He found that the ratio of transition Reynolds numbers for insulated and cooled-wall cases increased much faster than that experimentally measured. The results showed that LST alone was insufficient to determine the transition Reynolds number, and it was necessary to consider the properties of the environment disturbances. Balakumar et al. [5] investigated the evolution of small amplitude travelling disturbances in a rotating disk flow, where the disturbances were generated by perturbing the steady rotational speed of the disk and introducing roughness elements on disk surface. They found that only eigensolutions at frequencies larger than 4.58 times of the steady disk rotational frequency grew algebraically in radial direction. Their results of receptivity coefficient computations showed that these eigensolutions were excited the most when the width of roughness elements in radial direction was about the radial location of the roughness. By solving the nonlinear parabolized stability equations (PSE), Bertolotti [6] studied the amplification of vortices over a plate generated by surface roughness, blowing-suction, or both. The results showed that the growth of vorticity could be much larger with the presence of both wall inhomogeneities. Choudhari [7] studied the roughness-induced generation of stationary and nonstationary vortices in three-dimensional boundary layers over a sweep wing, where nonstationary vortices were induced with the presence of free-stream acoustic disturbances. The effects of acoustic-wave orientation and different types of roughness geometries were considered. It was found that maximum receptivity occurred when the velocity fluctuation of acoustic disturbance was aligned with the wave-number vector of nonstationary vortex mode. Hanifi et al. [8] investigated transient growth phenomena of boundary-layer flows with a series of Mach numbers from 0.1 to 4.5 using spectral collocation method. They found that maximum transient growth increased with Mach number and could be scaled with the square of local Reynolds number. Andersson et al. [9] numerically calculated the maximum transient growth for steady disturbances and concluded that optimal disturbances consisted of streamwise vortices. They also found that maximum transient growth scaled linearly with the distance from the leading edge. Herbert [10] considered the stability and transition of 3D boundary layers varying both in streamwise and spanwise directions by extending the PSE to 3D boundary layers. The analysis of cross-flow dominated flow showed that the vector of growth rates (α_i, β_i) cannot be solely determined from the local flow characteristics and careful attention must be paid to initial conditions. Reshotko [11] investigated the spatial transient growth by examining examples including Poiseuille flow, hypersonic blunt body paradox and distributed roughness effects. It was demonstrated that bypass transition could be explained by transient growth thoery. Fedorov and Khokhlov [1] studied the receptivity of a hypersonic boundary layer over a flat plate to wall disturbances using a combination of asymptotic method and numerical simulation. They investigated the receptivity mechanisms to different wall disturbances, i.e., wall vibrations, periodic blowing-suctions, and temperature disturbances. It was found that strong excitations occurred in local regions where forcing disturbances were resonant with boundary-layer wave modes. They also found that hypersonic boundary layers were more sensitive to blowing-suction disturbances than to wall vibrations and temperature disturbances. Reshotko and Tumin [12] developed a model of roughness-induced transition and studied it by applying spatial transient growth theory. Their computational results of nosetip transition successfully reproduced the trends of experimental data of Reda and passive nosetip technology (PANT). Forgoston and Tumin [13] studied a three-dimensional wave packet generated by a local temperature slot in a hypersonic boundary layer. They found that the solution to this initial-value problem could be expanded in a biorthogonal eigen-function system as a sum of discrete and continuous modes. Recently, Tumin [2] solved the receptivity problem of compressible boundary layers to three-dimensional wall perturbations with the help of the biorthogonal eigenfunction system. In case of receptivity to roughness

elements, there are counter rotating streamwise vortices, streaks at both sides of the hump, and a wake region downstream from the hump. In supersonic boundary layer, there exist large amplitude perturbations near the Mach waves generated by roughness elements.

Kendall [14] experimentally studied the origin and growth of natural fluctuations in zero pressure-gradient boundary layers of several Mach numbers ranging from 1.6 to 8.5. Substantial growths of flow fluctuations were observed within the laminar boundary layer in the early region where the boundary layer was predicted to be stable by LST. These fluctuations were found to be related to the sound field for hypersonic flows. The growth rates of these fluctuations in the region downstream of the initial growth were in a reasonable agreement with the LST results of Mack. Maslov and Seminov [15] experimentally investigated the receptivity of a supersonic boundary layer to artificial acoustic waves by utilizing two parallel flat plates as shown in Fig. 1. The acoustic waves generated by an electric discharge system on the lower plate radiated into the external flow and penetrated into the boundary layer of the upper plate as free-stream acoustic disturbances. It was found that the acoustic disturbances were converted into boundary-layer wave modes most efficiently at the leading edge, in the neighborhood of the acoustic branch of the neutral curve, and in the vicinity of lower branch of the neutral curve. A similar experiment was carried out at a Mach 5.92 flow by Maslov et al. [16] to study the leading edge receptivity of the hypersonic boundary layer. It was observed that Tollmien-Schlichting waves were generated by the acoustic waves impinging on the leading edge. They also found that the receptivity coefficients depended on wave inclination angles. Gaster et al. [17] measured the velocity disturbance in a flat plate boundary layer induced by a three-dimensional shallow bump oscillating at a frequency of 2 Hz. It was observed that the intensity of velocity disturbance reached its maximum near $\eta = 2$ at a location about 100 boundary-layer thickness downstream of the bump. They also noticed a small secondary peak in the spanwise spectrum near the bump. Bakchinov et al. [18] studied the stability of an incompressible boundary layer over a flat plate. The experiments were carried out in a low speed wind tunnel. Inside the boundary layer, roughness elements were arranged in spanwise direction to generate stationary streamvise vortices. Small amplitude travelling waves were introduced to the boundary layer on top of the steady vortices. According to their results, the maximum amplification of wave amplitude was found at a wall-normal position where the mean streamwise velocity was equal to wave phase velocity. In order to evaluate the optimal-disturbance theories, White [19] investigated the transient growth of a flat plate boundary layer to controlled stationary disturbances generated by using spanwise roughness array. The results showed quantitative differences between experimental measurements and theoretical predictions, which did indicate that realistic stationary disturbances could exhibit significant nonoptimal behavior. White and Ergin [20] further studied the receptivity and transient growth of a Blasius boundary layer to roughness-induced disturbances, where the initial disturbances were generated by a spanwise array of roughness elements. In experiments, detailed information on the disturbances and the transient growth was measured using hotwire instruments. The results indicated that energy associated with the roughness-induced disturbances scaled with the roughness-based Reynolds number. Fransson et al. [21] experimentally and theoretically investigated the transient growth of stationary streamwise streaks in a flat plate boundary layer. The stable laminar streaks was periodic in spanwise direction and was generated by a spanwise periodic array of small cylindrical roughness elements. The results showed that the maximum transient growth was mainly determined by the height of roughness elements. Recently, White et al. [22] investigated the effects of the amplitude and diameter of cylindrical roughness elements on transient growth features. Their experimental results showed that energy of stationary disturbances varied as Re_k^2, the square of roughness-based Reynolds number, and the qualitative nature of transient growth strongly depended on the roughness diameter.

With the development of advanced computers and numerical techniques, numerical simulation of the receptivity process by directly solving Navier-Stokes equations has become feasible. Kawamura et al. [23] analyzed incompressible high-Reynolds-number flows around a cylinder with surface roughness by integrating Navier-Stokes equations using finite difference method. In their computations, the height of roughness elements was half percent of the cylinder diameter. They observed a sharp drag-coefficient reduction near the Reynolds number of 20000. Joslin and Grosch [24] computed the disturbance velocity field downstream of a shallow bump in a laminar boundary layer by direct numerical simulation of incompressible Navier-Stokes equations. The flow conditions in their simulation was the same as the experimental parameters of Gaster et al. [17]. According to the simulation results, modal growth and decay trends of velocity disturbance were consistent with Gaster et al.'s experimental measurements. Bottaro and Zebib [25] numerically investigated the formation and growth of spatial Görtler vortices induced by wall roughness. In all naturally developing cases, the average spanwise wavelengths of vortices were close to those of optimal disturbances predicted by LST. Stemmer et al. [26] studied the laminar-turbulent transition mechanisms of a flat plate boundary layer to a harmonic point source disturbances by numerical simulations based on the Navier-Stokes equations for three-dimensional incompressible flow. The results for early stages agree very well with LST results and with in-flight experiments. Collis and Lele [27] numerically investigated the formation of stationary crossflow

vortices in a three-dimensional boundary layer due to surface roughness near the leading edge of a swept wing by solving the compressible Navier-Stokes equations. The results showed that convex surface curvature enhances receptivity while non-parallel effects strongly reduce the initial amplitude of stationary crossflow vortices. Malik et al. [28] investigated the responses of a Mach 8 flow over a sharp wedge of a half-angle of 5.3° to three types of external forcing: a planar free-stream acoustic wave, a narrow acoustic beam enforced on the bow shock near the leading edge, and a blowing-suction slot on the wedge surface. They concluded that these three types of forcing eventually result in the same type of instability waves in the boundary layer. Zhong [29] studied the acoustic receptivity of a hypersonic flow over a parabola by solving full Navier-Stokes equations. It was concluded that the generations of boundary-layer wave modes were mainly owing to the interaction of the boundary layer with the transmitted acoustic waves instead of entropy and vorticity waves. In a series of papers, Ma and Zhong [30, 31, 32] studied the receptivity mechanisms of a supersonic boundary layer to various free-stream disturbances by a combination of numerical simulation and linear stability theory. It was found that, in addition to the conventional first and second Mack modes, there existed a family of stable modes which played an important role in the excitation of unstable modes. Dong and Zhong [33] carried out parametric simulations of receptivity to free-stream disturbances of a Mach 15 flow over 3D blunt leading edges by using high-order shock-fitting finite difference method on parallel clusters. The results showed that the magnitude of transient growth inside the boundary layer increased by introducing random roughness strips on the wall. Egorov et al. [34] developed a numerical algorithm and applied it to the simulation of unsteady two-dimensional flows relevant to receptivity of supersonic and hypersonic boundary layers. For small forcing amplitudes, the second-mode growth rates obtained by numerical simulation agreed well with those predicted by LST including the non-parallel effects. The results of their simulations showed a non-linear saturation of fundamental harmonic and rapid growth of higher harmonics. Choudhari and Fischer [35, 36] examined the roughness-induced transient growth in a laminar boundary layer due to a spanwise periodic array of circular disks at the surface. The effects of roughness height, size, and shape on the transient growth were also explored. Their numerical simulation results indicated that energy levels of the dominant stationary disturbances were consistent with the Re_k^2 scaling of White et al. [22]. Spontaneous vortex shedding behind the roughness array was identified for sufficiently large roughness heights. Ma and Zhong [37] studied the receptivity mechanisms of the same hypersonic boundary layer as in Malik et al. [28] investigation to various free-stream disturbances, i.e., fast and slow acoustic waves, vorticity waves, and entropy waves, by solving the two-dimensional compressible Navier-Stokes equations. They found that the stable modes in the boundary layer played a very important role in the receptivity process. Wang and Zhong [38, 39] extended Ma and Zhong's [37] work to study the receptivity mechanisms of the same flow over the sharp wedge to periodic blowing-suction disturbances introduced in a narrow region on the wall. The effects of frequency, location, profile, and length of the blowing-suction actuator on the receptivity process are also investigated based on series of numerical simulations. The numerical results show that mode F, mode S, and acoustic modes are excited by the blowing-suction disturbances. Far downstream of the forcing region, mode S becomes the dominant mode in the boundary layer. All cases of numerical simulations consistently show that the synchronization point of mode F and mode S plays an important role in the excitation of mode S by wall blowing-suction. Mode S is strongly excited when the blowing-suction actuator is located upstream of the synchronization point. On the other hand, when the blowing-suction actuator is downstream of the synchronization point, there is a very weak excitation of mode S, despite the fact that the blowing-suction actuator is still within the unstable region of mode S. A concurrent theoretical study had been carried out by Tumim, Wang, and Zhong [40] to compare the theoretical and numerical results of receptivity coefficients and to analyze the receptivity characteristics. The perturbation flow field downstream of the blowing-suction actuator was decomposed into boundary-layer wave modes with the help of the biorthogonal eigenfunction system. It was found that there was a good agreement between normal-mode amplitudes calculated with the help of the theoretical receptivity model and those obtained by projecting the numerical results onto the normal modes. Zhong and Ma [41] numerically studied the receptivity to weak free-stream fast acoustic waves of a Mach 7.99 axisymmetric flow over a 7° half-angle blunt cone. They found that no Mack modes were excited by free-stream fast acoustic waves in the early region along the cone surface. The delay of the second-mode excitation was owing to the fact that the hypersonic boundary-layer receptivity was governed by a two-step resonant interaction process.

In this paper, the receptivity of a Mach 5.92 flat plate boundary layer to two and three-dimensional wall perturbations is investigated by numerical simulations and linear stability theory. Free-stream flow conditions of the hypersonic boundary layer are the same as those of Maslov et al.s [16] leading-edge receptivity experiments. The 2D steady base flow is simulated by solving two-dimensional compressible Navier-Stokes equations with a combination of a fifth-order shock-fitting finite difference method and a second-order TVD scheme. Three-dimensional steady base flow is extended from 2D base flow due to the fact that the flow field on a flat plate is independent of spanwise coordinate. The characteristics of boundary-layer wave modes are identified and evaluated by comparing the results

of LST and numerical simulations. Two-dimensional wall perturbations of six cases are introduced to 2D steady base flow by a forcing slot located on the flat plate. In order to investigate the transient growth phenomena, small-scale stationary three-dimensional roughness elements are introduced on the flat plate. The surface roughness is periodic in spanwise direction. Effect of thermal flat plate boundary conditions on the receptivity process is considered by comparing numerical simulations on adiabatic and isothermal flat plates, respectively.

2 Governing Equations and Numerical Methods

In the current numerical studies, a Mach 5.92 flow over a flat plate as shown in Figs. 2 and 3 is considered. The flow is assumed to be thermally and calorically perfect. The governing equations for the simulation are the full Navier-Stokes equations in the conservative form, i.e.,

$$\frac{\partial \vec{U}^*}{\partial t^*} + \frac{\partial}{\partial x_1^*}(\vec{F}_{1i}^* + \vec{F}_{1v}^*) + \frac{\partial}{\partial x_2^*}(\vec{F}_{2i}^* + \vec{F}_{2v}^*) + \frac{\partial}{\partial x_3^*}(\vec{F}_{3i}^* + \vec{F}_{3v}^*) = 0 \tag{1}$$

where the superscript "$*$" represents the dimensional variables. $\vec{U}^*$ is a vector containing the conservative variables of mass, momentum, and energy, i.e.,

$$\vec{U}^* = \{\rho^*, \rho^* u_1^*, \rho^* u_2^*, \rho^* u_3^*, e^*\} \tag{2}$$

The flux vector in Eq. (1) is divided into its inviscid and viscous components, because the two components are discretized with different schemes. The components, $\vec{F}_{1i}^*$, $\vec{F}_{2i}^*$, $\vec{F}_{3i}^*$, are inviscid flux vectors whereas $\vec{F}_{1v}^*$, $\vec{F}_{2v}^*$, and $\vec{F}_{3v}^*$ are viscous flux vectors. The flux vectors can be expressed as

$$\vec{F}_{ji}^* = \begin{bmatrix} \rho^* u_j^* \\ \rho^* u_1^* u_j^* + p^* \delta_{1j} \\ \rho^* u_2^* u_j^* + p^* \delta_{2j} \\ \rho^* u_3^* u_j^* + p^* \delta_{3j} \\ u_j^*(e^* + p^*) \end{bmatrix}, \quad \vec{F}_{jv}^* = \begin{bmatrix} 0 \\ -\tau_{1j}^* \\ -\tau_{2j}^* \\ -\tau_{3j}^* \\ -\tau_{1j}^* u_1^* - \tau_{2j}^* u_2^* - \tau_{3j}^* u_3^* + k^* \frac{\partial T^*}{\partial x_j^*} \end{bmatrix} \tag{3}$$

with $j \in \{1, 2, 3\}$. In Eq. (3), δ_{ij} $(i = 1, 2, 3)$ is the Kronecker Delta function. In the perfect gas assumption, pressure and energy are given by

$$p^* = \rho^* R^* T^* \tag{4}$$

$$e^* = \rho^* c_v^* T^* + \frac{\rho^*}{2}(u_1^{*2} + u_2^{*2} + u_3^{*2}) \tag{5}$$

where c_v^* is the specific heat at constant volume. For compressible Newtonian flow, the viscous stress tensor can be written as:

$$\tau_{ij}^* = \mu^*(\frac{\partial u_i^*}{\partial x_j^*} + \frac{\partial u_j^*}{\partial x_i^*}) - \frac{2}{3}\mu^*(\frac{\partial u_1^*}{\partial x_1^*} + \frac{\partial u_2^*}{\partial x_2^*} + \frac{\partial u_3^*}{\partial x_3^*})\delta_{ij} \tag{6}$$

with $i, j \in \{1, 2, 3\}$. In the simulation, the viscosity coefficient, μ^*, and the heat conductivity coefficient, k^*, are calculated using the Sutherland's law together with a constant Prandtl number, Pr. They are both functions of temperature only.

$$\mu^*(T^*) = \mu_r^* \left(\frac{T^*}{T_r^*}\right)^{3/2} \frac{T_r^* + T_s^*}{T^* + T_s^*} \tag{7}$$

$$k^*(T^*) = \frac{\mu^*(T^*) c_p^*}{Pr} \tag{8}$$

where $\mu_r^* = 1.7894 \times 10^{-5}$ Ns/m^2, $T_r^* = 288.0$ K, $T_s^* = 110.33$ K, and c_p^* is the specific heat at constant pressure. In this paper, the dimensional flow variables are non-dimensionalized by free-stream parameters. Specifically, density ρ^*, temperature T^*, velocities u_1^*, u_2^*, u_3^*, and pressure p^* are non-dimensionalized by ρ_∞^*, T_∞^*, u_∞^*, and $\rho_\infty^* u_\infty^{*2}$. Furthermore, x_1^* and x_3^* is non-dimensionalized by unit length in meter, whereas x_2^* is non-dimensionalized by the

local boundary-layer thickness, $\sqrt{\mu^*_\infty x^*_1/\rho^*_\infty u^*_\infty}$. Referring to the coordinate system shown in Fig. 3, x^*_1, x^*_2, and x^*_3 are x^*, y^*, and z^*, respectively. The three variables, u^*_1, u^*_2, and u^*_3, are velocities in streamwise, wall-normal, and spanwise directions.

The high-order shock-fitting finite difference method of Zhong [42] is used to solve the governing equations in a domain bounded by the bow shock and the flat plate. In orther words, the bow shock is treated as a boundary of the computational domain. The Rankine-Hugoniot relation across the shock and a characteristic compatibility relation coming from downstream flow field are combined to solve the flow variables behind the shock. The shock-fitting method makes it possible for the Navier-Stokes equations to be spatially discretized by high-order finite difference methods. Specifically, a fifth-order upwind scheme is used to discretize the inviscid flux derivatives. Meanwhile, a sixth-order central scheme is used to discretize the viscous flux derivatives. For three-dimensional simulations, flux derivatives of $\vec{F}^*_{3i}$ and $\vec{F}^*_{3v}$ in spanwise direction are calculated by Fourier collocation method to achieve high accuracy. By using the shock-fitting method, the interaction between the bow shock and perturbations induced by wall disturbances is solved as a part of solutions with the position and velocity of the shock front being taken as dependent flow variables. A three-stage semi-implicit Runge Kutta method of Zhong et al. [43] is used for temporal integration. In the leading edge region, there exists a singular point at the tip of the flat plate, which introduces numerical instability if the fifth-order shock-fitting method is used to simulate the flow. Therefore, the computational domain for the shock-fitting simulation starts from a very short distance downstream of the leading edge. A second-order TVD scheme of Zhong and Lee [44] is used to simulate the steady base flow in a small region including the leading edge to supply inlet conditions for the shock-fitting simulation. For receptivity simulations, two-dimensional wall perturbations and 3D small-scale roughness elements are introduced in a downstream region where the shock-fitting method is used.

The same numerical method has been used by Ma and Zhong in their receptivity studies of supersonic and hypersonic boundary layers over a flat plate and a sharp wedge to various free-stream disturbances [30, 31, 32, 37]. The good agreement between numerical and LST results indicates that the high-order shock-fitting finite difference method is accurate to simulate the receptivity problems of high-speed boundary-layer flows. The numerical method has also been validated in the theoretical study and comparison with numerical simulation of Tumin, Wang, and Zhong [40]. The numerical perturbation field downstream of the blowing-suction actuator is decomposed into boundary-layer wave modes with the help of the biorthogonal eigenfunction system. The filtered-out amplitudes of mode S and mode F agree well with the theoretical solutions of linear receptivity problem. The Fourier collocation method has been tested by Zhong [45] to study the receptivity of a Mach 6 flow over a flared cone to free-stream disturbances. The numerical results are compared with published experiment results. It is found that the steady base flow solutions agree very well with the experiment results. The wave numbers and growth rates of numerical solutions are reasonably similar to the LST results.

3 Flow Conditions and Forcing Model

The free-stream flow conditions for currently studied flow are the same as those used by Maslov et al.[16] in their experiments, i.e.,

$$
\begin{array}{ll}
M_\infty = 5.92\,, & T^*_\infty = 48.69K\,, \\
p^*_\infty = 742.76Pa\,, & Pr = 0.72\,, \\
f^* = 50kHz\,, & \mathrm{F} = 3.0\times10^{-5}\,, \\
Re^*_\infty = \rho^*_\infty u^*_\infty/\mu^*_\infty = 13\times10^6/m &
\end{array}
$$

The dimensional coordinate x^* can be converted to the dimensionless local Reynolds number by

$$Re_x = Re^*_\infty\ x^* \tag{9}$$

where Re^*_∞ is the unit Reynolds number defined as

$$Re^*_\infty = \rho^*_\infty u^*_\infty/\mu^*_\infty \tag{10}$$

In LST studies of boundary-layer flows, the Reynolds number based on the local length scale of boundary-layer thickness, L^*, is generally used. They are expressed as

$$R = \frac{\rho^*_\infty u^*_\infty L^*}{\mu^*_\infty},\quad L^* = \sqrt{\frac{\mu^*_\infty x^*}{\rho^*_\infty u^*_\infty}} \tag{11}$$

Hence, the relation between R and local Reynolds number Re_x is given by

$$R = \sqrt{Re_x} \tag{12}$$

For the simulation of 2D steady base flow, the wall is adiabatic, and the physical boundary condition of velocity on the flat plate is the non-slip condition. When 2D perturbations of wall oscillation and wall blowing-suction are enforced on the steady base flow, the isothermal temperature condition, which is a standard boundary condition for theoretical and numerical studies of high frequency disturbances, is applied on the wall. Meanwhile, non-slip condition is applied on the wall except the forcing region where streamwise or wall-normal velocity disturbances are introduced. On the other hand, when 2D temperature perturbation is enforced, the isothermal temperature condition is applied on the wall except the forcing region. Meanwhile, non-slip condition is applied on the wall. For three-dimensional stationary roughness elements, the computational domain and grid structure of receptivity simulation are the same as those of base flow simulation by transferring boundary conditions from rough wall to undisturbed surface. Boundary conditions of temperature and velocities on the lowest grid line are specified according to the model of roughness elements. Inlet conditions are specified, while high-order extrapolation is used for outlet conditions because the flow is hypersonic at the exit boundary except a small region near the flat plate.

In Maslov et al.'s[16] experiments, leading-edge receptivity of the Mach 5.92 flow on a flat plate to both two-dimensional and three-dimensional disturbances is investigated. An electric pulse generator with the center located at $x^* = 35$ mm is used to introduce disturbances to the steady base flow. It generates high-voltage electric pulses with duration of 2μs and a frequency of 50 kHz. Experimental results show that the disturbances are introduced by a local glow discharge through an aperture on the source plate when the voltages on the electrodes are low (600 V). On the other hand, when the voltages on the electrodes are increased to 700 V, the size of the glow discharge increases and a flat streamwise extended oval is also observed. Maslov et al. analyzed the properties of the forcing disturbances and concluded that the glow discharge introduces disturbances through a blowing-suction mechanism whereas the flat oval on the plate introduces thermal energy. For numerical simulations in this paper, we study the receptivity of the Mach 5.92 flat plate boundary layer to two and three-dimensional wall perturbations, which is schematically shown in Figs. 2 and 3.

According to the properties of the electric pulse generator used in Maslov et al.'s experiments, a model of 2D wall perturbations is proposed in this paper, which consists of streamwise velocity, wall-normal mass flux, and temperature perturbations. The model can be mathematically expressed as

$$\begin{pmatrix} u^{*\prime} \\ (\rho v)^{*\prime} \\ T^{*\prime} \end{pmatrix} = \begin{pmatrix} Q_u \epsilon_1 F(l_1) u_w^{*\prime} \\ Q_v \epsilon_2 G(l_2)(\rho u)_\infty^* \\ Q_T \epsilon_3 H(l_3) T_\infty^* \end{pmatrix} S(t^*) \tag{13}$$

where $u_w^{*\prime} = (du^*/dy^*)_{y^*=0}$ is the derivative of streamwise velocity on the plate of the steady base flow. $(\rho u)_\infty^*$ and T_∞^* are the mass flux and temperature in free-stream, respectively. And Q_u, Q_v, and Q_T are three constants with the value of either 1 or 0. The combination of (Q_u, Q_v, Q_T) determines specific wall perturbations. For example, (1, 0, 0) is the case of wall oscillation, (0, 1, 0) is the case of blowing-suction on the plate, whereas (0, 0, 1) is the case of temperature perturbation on the wall. Variables of ϵ_1, ϵ_2, and ϵ_3 are small parameters representing the dimensionless amplitudes of perturbations. $F(l_1)$, $G(l_2)$, and $H(l_3)$ are the profile functions of perturbations. The variables l_1, l_2, and l_3 are dimensionless coordinates defined within the forcing region ($x_i^* \le x^* \le x_e^*$), where x_i^* and x_e^* are the coordinates of the leading and trailing edges of the forcing region. In Maslov et al's experiments, x_i^* and x_e^* are equal to 33 mm and 37 mm, respectively. $S(t^*)$ is a time-periodic step function defined as

$$S(t^*) = \begin{cases} 1.0 & \text{if } mod(t^*, 20\mu\text{s}) \le 2\mu\text{s} \\ 0.0 & \text{if } mod(t^*, 20\mu\text{s}) \ge 2\mu\text{s} \end{cases} \tag{14}$$

where *mod* is a residual function. The value 20μs is the period of 2D wall perturbation at a frequency of $f^* = 50$ kHz. Figure 4 plots the time-periodic step function $S(t^*)$ versus time t^* for five periods. It shows that the perturbations are introduced to the steady base flow only within a short time of 2μs in a period of 20μs, because the electric pulse used in the experiments has a duration of 2μs.

The circular frequency of 2D wall perturbations is related to the frequency by

$$\omega^* = 2\pi f^* \tag{15}$$

The circular frequency, ω^*, and the frequency, f^*, are non-dimensionalized according to

$$\omega = \frac{\omega^* L^*}{u_\infty^*} \tag{16}$$

$$F = \frac{2\pi f^* \mu_\infty^*}{\rho_\infty^* u_\infty^{*2}} = \frac{\omega^* \mu_\infty^*}{\rho_\infty^* u_\infty^{*2}} \tag{17}$$

With the definitions of Reynolds number R and the dimensionless frequency F, the dimensionless circular frequency can also be expressed as

$$\omega = RF \tag{18}$$

The profile function of the streamwise velocity perturbation, $F(l_1)$, can be expressed as

$$F(l_1) = -(20.25l_1^5 - 35.4375l_1^4 + 15.1875l_1^2)/2.45688 \tag{19}$$

where the variable l_1 is defined as

$$l_1 = 0.620287 \times \begin{cases} 2(x^* - x_i^*)/(x_e^* - x_i^*) & \text{if } x^* \le 35\text{mm} \\ 2(x_e^* - x^*)/(x_e^* - x_i^*) & \text{if } x^* \ge 35\text{mm} \end{cases} \tag{20}$$

In Eq. (19), the constant of 2.45688 is the value of $F(l_1)$ at $l_1 = 0.620287$, which is used to normalize the profile function. Figure 5 shows the profile function $F(l_1)$ and the variable l_1 within the forcing region. It is clearly shown that both $F(l_1)$ and l_1 are symmetric within the region 33 mm $\le x^* \le$ 37 mm. The negative values of $F(l_1)$ indicate that the streamwise velocity perturbation is towards the leading edge of the flat plate. It also shows that the specific 5th-order-polynomial profile function makes the perturbation at the edges (x_i^* and x_e^*) smooth.

The profile function of blowing-suction perturbation, $G(l_2)$, is the same as what we have used in the receptivity study of a Mach 8 flow over a sharp wedge to wall blowing-suction [38, 39], i.e.,

$$G(l_2) = \frac{1}{2.45688} \begin{cases} 20.25l_2^5 - 35.4375l_2^4 + 15.1875l_2^2 & \text{if } l_2 \le 1 \\ -20.25(2 - l_2)^5 + 35.4375(2 - l_2)^4 - 15.1875(2 - l_2)^2 & \text{if } l_2 \ge 1 \end{cases} \tag{21}$$

with the variable l_2 being expressed as

$$l_2 = \frac{2(x^* - x_i^*)}{x_e^* - x_i^*} \tag{22}$$

Again, the constant of 2.45688 in Eq. (21) is the value of the profile function at $l_2 = 0.620287$, which is used to normalize $G(l_2)$. Figure 6 shows the profile function $G(l_2)$ and the variable l_2 within the forcing region. The figure shows that $G(l_2)$ is anti-symmetric within the region 33 mm $\le x^* \le$ 37 mm whereas l_1 is linear. The specific 5th-order-polynomial profile function makes the perturbation at the edges (x_i^* and x_e^*) smooth. Due to the anti-symmetric property of the profile function, the net mass flux introduced to the boundary layer is zero at any instant.

In the current study, four different profile functions of temperature perturbation are tested. They are defined as $H_1(l_3)$, $H_2(l_3)$, $H_3(l_3)$, and $H_4(l_3)$, respectively. For $H_1(l_3)$, the profile of temperature perturbation is the reverse of the streamwise velocity perturbation given by Eq. (19), i.e., the temperature perturbation is positive within the forcing region.

$$H_1(l_3) = (20.25l_3^5 - 35.4375l_3^4 + 15.1875l_3^2)/2.45688 \tag{23}$$

The constant of 2.45688 is the value of $H_1(l_3)$ at $l_3 = 0.620287$, which is used to normalize the profile function. The variable l_3 is defined exactly the same as l_1 in Eq. (20).

For $H_2(l_3)$, the temperature perturbation is assumed to be uniformly distributed within the forcing region. Therefore, the profile function is expressed as

$$H_2(l_3) = 1.0 \tag{24}$$

where l_3 can be an arbitrarily defined dimensionless coordinate. As an example, it can be defined as

$$l_3 = \frac{x^* - x_i^*}{x_e^* - x_i^*} \tag{25}$$

In the third test case, $H_3(l_3)$ is mathematically expressed as

$$H_3(l_3) = (1.0 - \cos(\pi l_3))/2 \tag{26}$$

where l_3 is defined as

$$l_3 = \begin{cases} 2(x^* - x_i^*)/(x_e^* - x_i^*) & \text{if } x^* \le 35\text{mm} \\ 2(x_e^* - x^*)/(x_e^* - x_i^*) & \text{if } x^* \ge 35\text{mm} \end{cases} \tag{27}$$

The fourth profile function of temperature perturbation, $H_4(l_3)$, is expressed as

$$H_4(l_3) = \frac{erf(2.6/\sqrt{2}) - erf(l_3/\sqrt{2})}{erf(2.6/\sqrt{2})} \tag{28}$$

where erf is the error function. The dimensionless coordinate l_3 is defined as

$$l_3 = 2.6 - 2.6 \times \begin{cases} 2(x^* - x_i^*)/(x_e^* - x_i^*) & \text{if } x^* \leq 35\text{mm} \\ 2(x_e^* - x^*)/(x_e^* - x_i^*) & \text{if } x^* \geq 35\text{mm} \end{cases} \tag{29}$$

In Eqs. (28) and (26), the two constants, $erf(2.6/\sqrt{2}))$ and 2, are used to normalize the profile functions. Figure 7 compares the profile functions of the four different temperature perturbations. The figure shows that the profile functions are all normalized to having the maximum values of 1. However, the energy introduced to the steady base flow has the maximum for $H_2(l_3)$ and the minimum for $H_4(l_3)$, because it is proportional to the area surrounded by the profile function and the x^* axis.

In Dong and Zhong's [33] numerical simulations of transient growth in a Mach 15 boundary layer over a blunt leading edge, two types of 3D surface roughness models are introduced. In the first surface roughness model, inhomogeneous wall-normal velocity is applied on the surface with the mass conservation being enforced. Components of the randomly distributed small inhomogeneous velocity can be expressed as

$$\begin{cases} u_{wall}^* = \epsilon f(x^*, z^*) V^* \sin\theta \\ v_{wall}^* = \epsilon f(x^*, z^*) V^* \cos\theta \\ w_{wall}^* = 0 \end{cases} \tag{30}$$

where ϵ is the amplitude parameter whereas V^* is the inhomogeneous wall-normal velocity. As a random function between $(-1,\ 1)$, $f(x^*, z^*)$ has the property of $\sum f(x^*, z^*) = 0$, enforcing the mass conservation condition. The angle of θ is defined between the tangential direction of the surface and the x^* axis. According to this model, inhomogeneous wall-normal velocity is directly applied to the rough wall, which indicates that the specific roughness geometry needs to be considered in numerical simulations. However, it is hard for numerical simulations to using grid structures attached to the geometries of complex roughness elements.

The second surface roughness model is derived with the assumption of small height of the roughness elements. Due to the existence of roughness, the wall surface changes from $y^* = 0$ to $y^* = \epsilon\hbar^*(x^*, z^*)$, where $\hbar^*(x^*, z^*)$ is a given function representing the profile of roughness elements. The parameter of ϵ is used to adjust the height. The physical non-slip conditions of velocity on the rough wall are

$$\begin{cases} u^*(x^*, \epsilon\hbar^*(x^*, z^*), z^*) = 0 \\ v^*(x^*, \epsilon\hbar^*(x^*, z^*), z^*) = 0 \\ w^*(x^*, \epsilon\hbar^*(x^*, z^*), z^*) = 0 \end{cases} \tag{31}$$

Under the linear assumption of small-height roughness elements, boundary conditions on the rough wall can be transferred to the undisturbed surface by a Talyor expansion, i.e.,

$$\begin{cases} u^*(x^*, 0, z^*) = -\epsilon\hbar^*(x^*, z^*) \frac{\partial u^*}{\partial y^*} \mid_{y^*=0} \\ v^*(x^*, 0, z^*) = -\epsilon\hbar^*(x^*, z^*) \frac{\partial v^*}{\partial y^*} \mid_{y^*=0} \\ w^*(x^*, 0, z^*) = -\epsilon\hbar^*(x^*, z^*) \frac{\partial w^*}{\partial y^*} \mid_{y^*=0} \end{cases} \tag{32}$$

In order to investigate the effect of thermal flat plate boundary conditions on the receptivity to roughness elements, both isothermal and adiabatic temperature conditions are considered. For small-height roughness, the temperature conditions on rough wall are expressed as

$$\begin{cases} T^*(x^*, \epsilon\hbar^*(x^*, z^*), z^*) = T_{wall}^* & \text{isothermal} \\ \\ \frac{\partial T^*(x^*, \epsilon\hbar^*(x^*, z^*), z^*)}{\partial y^*} = 0 & \text{adiabatic} \end{cases} \tag{33}$$

Similarly, the temperature conditions can be transferred to undisturbed surface as follows:

$$\begin{cases} T^*(x^*, 0, z^*) = T_{wall}^* - \epsilon\hbar^*(x^*, z^*) \frac{\partial T^*}{\partial y^*} \mid_{y^*=0} & \text{isothermal} \\ \\ \frac{\partial T^*(x^*, 0, z^*)}{\partial y^*} = -\epsilon\hbar^*(x^*, z^*) \frac{\partial^2 T^*}{\partial y^{*2}} \mid_{y^*=0} & \text{adiabatic} \end{cases} \tag{34}$$

In Eqs. (32) and (34), all derivatives on the right-hand-side of equations are calculated using the undisturbed steady base flow. Furthermore, T^*_{wall} in Eqs. (34) and (33) are the wall temperature of undisturbed steady base flow.

For the stationary roughness elements considered in current paper, the function of $\hbar^*(x^*, z^*)$ is define as

$$\hbar^*(x^*, z^*) = \hbar^*(l_4)\cos(\beta^* z^*) \tag{35}$$

where β^* is the wave number in spanwise direction. The function $\hbar^*(l_4)$ and the variable l_4 are defined similar to Eqs. (23) and (20). They are expressed as

$$\hbar^*(l_4) = (20.25l_4^5 - 35.4375l_4^4 + 15.1875l_4^2)/2.45688 \tag{36}$$

$$l_4 = 0.620287 \times \begin{cases} 2(x^* - x_i^*)/(x_e^* - x_i^*) & \text{if } x^* \le 4.28125\text{mm} \\ 2(x_e^* - x^*)/(x_e^* - x_i^*) & \text{if } x^* \ge 4.28125\text{mm} \end{cases} \tag{37}$$

The coordinates of the leading and trailing edges of the roughness elements in streamwise direction, x_i^* and x_e^*, are equal to 3.3125 mm and 5.25 mm, respectively. The constant of 2.45688 is the value of $\hbar^*(l_4)$ at $l_4 = 0.620287$, which is used to normalize the profile function. Figure 8 shows the profile function $\hbar^*(l_4)$ and the variable l_4 of the roughness element in streamwise direction.

4 Results and Discussions

4.1 Steady base flow

The 2D steady base flow over the flat plate is simulated by solving the two-dimensional compressible Navier-Stokes equations with a combination of a fifth-order shock-fitting finite difference method and a second-order TVD scheme. In the leading edge region, there exists a singular point at the tip of the plate, which will introduce numerical instability if the fifth-order shock-fitting method is used to simulate the flow. Therefore, the computational domain for the fifth-order shock-fitting method starts at $x^* = 0.0025$ m and ends at $x^* = 0.879$ m, corresponding to $R = 180.28$ and $R = 3380.38$, respectively. In actual simulations, the computational domain is divided into 19 zones with a total of 3746 grid points in streamwise direction. The number of grid points in wall-normal direction is 121 before $x^* = 0.309$ m and 176 after that position. Forty-one points are used in the overlap region between two neighboring zones, which is proved to be sufficient to make the solution accurate and smooth within the whole domain. An exponential stretching function is used in the wall-normal direction to cluster more points inside the boundary layer. On the other hand, the grid points are uniformly distributed in streamwise direction. The spatial convergence of the results based on this grid structure has been evaluated by grid refinement studies to ensure the grid independence of the fifth-order shock-fitting simulations.

For the first zone of the shock-fitting calculations, the inlet conditions are obtained from the results of the second-order TVD shock-capturing scheme which is used to simulate the steady base flow in a small region including the leading edge. For other zones, inlet conditions are interpolated from the results of the previous zone. The computational domain for the second-order TVD scheme starts at $x^* = -0.0005$ m and ends at $x^* = 0.0035$ m. Three sets of grid structures are used to check the grid independence of the numerical results. Figure 9 compares the density contours of flow field simulated based on the three sets of grid structures. It shows that the dashdot contours agree well with the dashed contours whereas they have discrepancies with the solid contours. This figure indicates that the grid structure of 201×176 is enough to ensure the grid independence. However, the grid structure of 161×101 is too coarse to achieve spatially converged numerical results.

Figures 10 and 11 show the density and wall-normal velocity contours of the steady base flow over the flat plate obtained from the second-order TVD scheme and the fifth-order shock-fitting method, respectively. The flow field including the leading edge is simulated by the TVD scheme, while the flow field after $x^* = 0.0025$ m is simulated by the shock-fitting method. These figures show that density and wall-normal velocity contours of the two methods have a good agreement near the leading edge of the buffering region, which indicates that the TVD solutions are accurate enough to be used as inlet conditions for the fifth-order shock-fitting simulation in the first zone. The small discrepancies of the contours near the bow shock are due to viscous effect. Because of the viscosity, the bow shock has a finite thickness for TVD simulation, while it is infinitely thin for the shock-fitting simulation. The combination of the shock-fitting method and the TVD scheme has also been validated in cases of supersonic and hypersonic steady base flows by Ma & Zhong[46] and Wang & Zhong[39].

Figure 12 shows the pressure contours of the steady base flow simulated by the fifth-order shock-fitting finite difference method. The upper boundary of the flow field represents the bow shock induced by the displacement thickness of the boundary layer. The lower boundary is the surface of the flat plate. A part of the pressure field

from $x^* = 0.03$ m to $x^* = 0.08$ m is amplified to show clearly the pressure contour within the boundary layer. It is noticed that pressure is approximately a constant across the boundary layer and along the Mach lines, which is consistent with the theories of the boundary layer flow and inviscid supersonic aerodynamics. At a fixed location (constant x^*), pressure behind the shock is higher than that on the flat plate due to the existence of the bow shock. Figure 13 shows the pressure distributions on the flat plate and behind the bow shock obtained by the fifth-order shock-fitting method. Near the leading edge, there exists great pressure gradient for the numerical result, which is caused by the interaction between the inviscid outer flow and the viscous boundary layer. From upstream to downstream, the outer-flow/boundary-layer interaction becomes weaker with the bow shock moving away from the boundary layer. As a result, the pressure approaches a constant value further downstream with the pressure gradient decreasing. Again, Fig. 13 shows that the pressure behind the shock is higher than that on the plate at a fixed location (constant x^*).

In order to evaluate the accuracy of numerical simulation, the steady base flow simulated by the fifth-order shock-fitting method is compared with the experimental results. According to Maslov et al.'s experiments, the effect of the inviscid/viscous interaction is strong within the region 0.2 mm $< x^* <$ 33 mm. Figure 13 shows that pressure on the flat plate and behind the shock have large gradients upstream of the location of $x^* = 50$ mm, which is consistent with the experiments. More comparisons of the steady base flow between numerical simulations and Maslov et al.'s experiments had been made in a previous paper [47]. It is found that the numerical results agree well with the experimental results.

Due to the fact that the flow field on a flat plate is independent of spanwise coordinate, three-dimensional steady base flow is extended from 2D base flow. Figures 14 and 15 show the pressure contours in spanwise and streamwise cross-sections of the 3D base flow extended from 2D steady base flow. In Fig. 14, pressure contours in a cross-section is similar to those of 2D base flow as shown in Fig. 12, i.e., pressure is a constant across the boundary layer and along the Mach lines. In Fig. 15, pressure is a constant in spanwise direction, because the base flow over a flat plate is independent of spanwise coordinate. Both figures show that, at a fixed location (constant x^*), the pressure behind the shock is higher than that on the plate due to the existence of the bow shock, which indicates that 3D base flow is successfully extended from 2D steady base flow.

4.2 Characteristics of boundary-layer normal mode

The characteristics of boundary-layer wave modes of the Mach 5.92 flow on a flat plate is studied by LST based on a multi-domain spectral method of Malik [48]. The LST code was written by Ma and Zhong [30]. The velocity, pressure, and temperature disturbances are represented by harmonic waves of the form

$$\begin{Bmatrix} \tilde{u} \\ \tilde{v} \\ \tilde{w} \\ \tilde{p} \\ \tilde{T} \end{Bmatrix} = \begin{Bmatrix} \hat{u}(y) \\ \hat{v}(y) \\ \hat{w}(y) \\ \hat{p}(y) \\ \hat{T}(y) \end{Bmatrix} e^{i(\alpha_c x + \beta_c z - \omega_c t)} \tag{38}$$

The parameters of α_c and β_c are wave number components in streamwise and spanwise directions, and ω_c is the circular frequency. For two-dimensional wall perturbations, $\beta_c = 0$. Substituting disturbances of Eq. (38) and the 2D steady base flow into the compressible linearized Navier-Stokes equations, an ordinary-differential-equation system is achieved, i.e.,

$$(A\frac{d^2}{dy^2} + B\frac{d}{dy} + C)\phi = 0 \tag{39}$$

where ϕ is the disturbance vector defined by $\{\hat{u}, \hat{v}, \hat{p}, \hat{T}, \hat{w}\}$. The coefficient matrices of A, B, and C are given in Malik's paper [48]. In spatial stability analysis, the two parameters, ω_c and β_c, are specified as real numbers. The streamwise wave number, α_c, is a complex number and solved as the eigenvalue of the ordinary-differential-equation system. The complex wave number α_c can be expressed as

$$\alpha_c = \alpha_r + i\alpha_i \tag{40}$$

where α_i is the local growth rate. A boundary-layer wave mode is unstable when $\alpha_i < 0$ whereas it is stable when $\alpha_i > 0$. The real part, α_r, is the local wave number which can be used to define the local phase velocity:

$$a = \frac{\omega_c}{\alpha_r} \tag{41}$$

Both the wave number and the phase velocity can be used to identify the boundary-layer wave mode.

The steady base flow needed for the LST analysis can be obtained either by numerically solving Navier-Stokes equations or by computing a self-similar boundary-layer solution. Although the numerical result is more accurate than the self-similar solution, it is inconvenient to use numerical steady base flow for the LST analysis at series of locations. Therefore, the self-similar boundary-layer solution is used in the study of LST.

Figure 16 shows the streamwise velocity and temperature profiles in the wall-normal direction at the location of $x^* = 0.159$ m ($R = 1437.71$). The current numerical solutions are compared with the corresponding self-similar boundary-layer solutions in the figure. The corresponding profiles of first- and second-order derivatives of streamwise velocity and temperature are compared in Figs. 17 and 18, respectively. These three figures show that the self-similar boundary-layer solution agrees very well with the current numerical solution. The only exception is the small difference in the second-order derivatives of the streamwise velocity and temperature near the edge of the boundary layer. It was tested by Ma and Zhong [30] that the linear stability characteristics based on the self-similar boundary-layer solution were very close to those based on the numerical mean flow solution, although the outer-flow/boundary-layer interaction is neglected in the self-simliar boundary-layer solution. Therefore, the self-similar boundary-layer solution is acceptable to be used to investigate the characteristics of the boundary-layer wave modes in this paper.

Figure 19 shows eigenvalue spectra of the boundary-layer wave modes for a case with dimensionless frequency of $F = 53.03 \times 10^{-6}$ ($f^* = 100$ kHz) at $x^* = 0.189$ m ($R = 1567.48$). This frequency is the second harmonic of the 2D wall perturbation. The figure shows the wave spectra corresponding to fast acoustic mode, vorticity or entropy mode, and slow acoustic mode. The two discrete modes in the figure marked by circles are mode F and mode S, which is validated by the corresponding eigenfunctions of u'_r and p'_r as shown in Figs. 20 and 21. The two figures show that the eigenfunctions are approximately equal to zero out of the boundary layer, which indicates that the two discrete modes exist in the boundary layer. Mode F is a stable mode, which was called Mode I by Ma and Zhong [30, 31]. This mode originates from the fast acoustic spectrum on the left side of the figure and passes the entropy and vorticity spectrum at the center as dimensionless frequency increases. Mode S originates from the slow acoustic spectrum on the right side of the figure. It becomes unstable in certain range of dimensionless frequency. The figure also shows that mode S at the frequency of $f^* = 100$ kHz is unstable at $x^* = 0.189$ m with $\alpha_i < 0$.

For hypersonic boundary layer flow, mode S is the dominant instability wave. Therefore, characteristics of mode S is of critical importance to understand receptivity and transition mechanisms. Figure 22 shows the dimensionless phase velocity of mode S at two locations of $x^* = 0.159$ m and $x^* = 0.159$ m as a function of the dimensionless circular frequency ω. The three dashed lines represent the dimensionless phase velocities of fast acoustic mode ($a = 1 + M_\infty^{-1}$), vorticity or entropy mode ($a = 1$), and slow acoustic mode ($a = 1 - M_\infty^{-1}$), respectively. The excellent agreement of the phase velocities at different locations indicates that the phase velocity is approximately a function of ω only. The figure clearly shows that mode S originates from slow acoustic mode.

Figure 23 shows the growth rates of mode S at the same set of locations as a function of the dimensionless circular frequency ω. The horizontal dotted line stands for the neutral modes ($\alpha_i = 0$). In Fig. 23, the growth rates of mode S of the two locations agree well, and they are approximately functions of ω only. Mode S is unstable in the region from $\omega_I = 0.00827$ to $\omega_{II} = 0.18465$. For unstable mode S, it is also noticed that the growth rate upstream of $\omega = 0.095$ is much larger than those around and downstream of it. This indicates that mode S is more unstable around and downstream of $\omega = 0.095$. The parameters ω_I and ω_{II} are called the Branch I and Branch II neutral points of mode S. The figure shows that mode S is stable upstream of Branch I neutral point and downstream of Branch II neutral point. The locations of the Branch I and Branch II neutral points in x^* coordinate, which changes with different dimensionless frequencies, can be calculated by

$$x_I^* = \frac{(\omega_I/F)^2}{Re_\infty^*} \tag{42}$$

$$x_{II}^* = \frac{(\omega_{II}/F)^2}{Re_\infty^*} \tag{43}$$

Equations (42) and (43) shows that when F increases, the corresponding x_I^* and x_{II}^* decrease. In other words, the Branch I and Branch II neutral point move upstream when F increases. Table 1 lists the locations of the Branch I and Branch II neutral points, x_I^* and x_{II}^*, for the base frequency and its first 14 harmonics.

4.3 Receptivity to 2D wall perturbations

The receptivity results of the hypersonic boundary layer to 2D wall perturbations are presented in this section. Forcing perturbations are introduced to the steady base flow through a slot on the plate with the leading and

trailing edges at $x_i^* = 33$ mm and $x_e^* = 37$ mm. Specifically, six cases of wall perturbations are considered. In each case, the frequency of perturbation is equal to 50 kHz. The values of ϵ_1, ϵ_2 and ϵ_3 in Eq. (13) are assigned to be 1.0×10^{-7}, 1.0×10^{-5}, and 1.0×10^{-3}, respectively. The subsequent responses of the hypersonic boundary layer are simulated by the fifth-order shock-fitting method. Details of wall perturbations for the six cases are listed in Tables 2 and 3.

Table 2 shows that case 1 is the case of wall oscillation, case 2 is the case of blowing-suction, whereas cases $3 \sim 6$ are the cases of temperature perturbations on the wall. In Table 3, the dimensional amplitudes of the six cases of wall perturbations are obtained from Eq. 13. They are non-dimensionalized by the corresponding free-stream variables: $u_\infty^* = 827.974$ m/s, $(\rho u)_\infty^* = 44.01$ kg/m^{2}s, and $T_\infty^* = 48.69$ K, respectively. The amplitudes of the temperature perturbations of cases $3 \sim 6$ are the same, because the profile functions of $H_1(l_3)$, $H_2(l_3)$, $H_3(l_3)$, and $H_4(l_3)$ are all normalized to have the maximum values being 1, which is shown clearly in Fig. 7.

To get the overall feature of the simulated unsteady flow field, Fig. 24 shows the contours of the instantaneous pressure perturbation induced by 2D wall oscillation at a frequency $f^* = 50$ kHz (case 1). After the forcing region, the excited pressure perturbations are divided into two branches. One branch radiates into the external flow outside the boundary layer and propagates along the Mach lines (acoustic modes), while the other branch stays within the boundary layer (mode F and mode S). Far downstream of the forcing region, mode F decays owing to its inherent stability whereas mode S grows substantially because of its instability. Therefore, mode S becomes the dominant mode in the boundary layer. The wave structure in the boundary layer is typical of mode S for hypersonic flows. Similar characteristics of instantaneous pressure perturbation contours are consistently shown in cases from 2 to 6. Figure 25 shows the distribution of dimensionless instantaneous pressure perturbation along the flat plate in case 1. The amplification of the pressure perturbation from upstream to downstream indicates the excitation of unstable modes in the boundary layer. It is very likely that mode S is excited in the boundary layer by wall oscillation. The standing wave structures indicate the modulations between boundary-layer wave modes at different frequencies. It is also shown in Fig. 25 that the significant increase of pressure perturbation starts around the location of $x^* = 0.35$ m.

In order to check the properties of the unstable modes, a Fourier transform is applied to the dimensionless instantaneous pressure perturbation along the flat plate. In the Fourier domain, the base freqency of 50 kHz and its higher harmonics are considered. All the frequencies can be expressed as

$$f_n^* = nf^* = 50n \quad \text{kHz} \tag{44}$$

where $n \in \{1, 15\}$. f_1^* is the base frequency whereas the other fourteen frequencies are higher harmonics. FFT of the instantaneous pressure perturbation leads to

$$p'(x^*, t^*) = \Sigma |p'_n(x^*)| e^{i[\phi'_n(x^*) - \omega_n^* t^*]} \tag{45}$$

where $p'(x^*, t^*)$ represents the dimensionless instantaneous pressure perturbation along the flat plate. In above equation, $|p'_n(x^*)|$ and $\phi'_n(x^*)$ are the perturbation amplitude and phase angle of the nth harmonic, respectively. Once $|p'_n(x^*)|$ and $\phi'_n(x^*)$ are achieved, a local wave number (α_{rn}) and a local growth rate (α_{in}) of the perturbation at the frequency of f_n^* can be calculated by

$$\alpha_{rn} = L^* \frac{d\phi'_n}{dx^*} \tag{46}$$

$$\alpha_{in} = -\frac{L^*}{|p'_n|} \frac{d|p'_n|}{dx^*} \tag{47}$$

where L^* is the length scale of local boundary layer thickness as defined by Eq. (11). The parameters of α_{rn} and α_{in} will represent the true wave number and growth rate only if the disturbance is dominated by a single wave mode. Otherwise, the disturbance needs to be decomposed in odrer to check properties of a specific mode. For example, Tumin, Wang, and Zhong [40] decomposed the disturbance at a location just downstream of the blowing-suction actuator with a biorthogonal eigenfunction system, where mode F, mode S, and acoustic modes coexisted and none of them was dominant.

Since our focus is on numerical simulation results, we only consider the later stage where mode S is the dominant mode in the boundary layer. In this case, Eqs. (46) and (47) can be used to check the properties of the unstable mode S. Figures 26, 27, and 28 show amplitudes of pressure perturbations along the flat plate at the base frequency and its first 14 harmonics in case 1. It is noticed that only perturbations at frequencies of f_n^* ($n < 6$) as shown in Fig. 26 have apparent amplitude growths downstream of the forcing region. The perturbation at the frequency

of f_1^* grows very slowly, whereas the perturbations at frequencies of f_n^* $(1 < n < 6)$ start to decrease far before reaching the corresponding Branch II neutral points predicted by LST. The higher harmonics shown in Figs. 27 and 28 decrease monotonically. Figure 29 compares numerical growth rate and LST growth rate of the pressure perturbation at the frequency of f_2^*. The growth rate of the simulation result has a good agreement with the LST growth rate in the region from $\omega = 0.11$ to $\omega = 0.13$. When ω is larger than 0.13, the growth rates from simulation are larger than those from LST, i.e., mode S obtained by the numerical simulation becomes more stable than that predicted by LST. As a result, the numerical perturbation starts to decrease far before the LST predicted Branch II neutral point, which is also shown in Fig. 26. For example, for the case of $n = 3$, the amplitude of pressure perturbation should keep increasing until $x^* = 0.37610$ m corresponding to the Branch II neutral point of mode S predicted by LST. However, the numerical perturbation stops increasing at the locatioin $x^* = 0.2$ m, far upstream of the LST predicted location. Such results are consistently found in all cases of receptivity simulations considered in the current study. The difference between growth rates of LST and simulation downstream of $\omega = 0.13$ may be caused by the effects of the non-parallel boundary-layer flow, the pressure gradient, and the bow shock. These factors are neglected in LST analysis.

Figure 29 compares wave number of the perturbation obtained from simulation at the frequency of f_2^* with that of LST. The good agreement of the two sets of wave numbers in downstream region of $\omega > 0.09$ confirms that mode S is the dominant mode in the boundary layer. The perturbation at the frequency of f_1^* starts to increase slowly, because mode S is slightly unstable upstream. The agreement in α_r is not so good in early region because mode F, mode S, and acoustic modes coexist in the boundary layer. In order to check the properties of mode S, the perturbation in early region needs to be decomposed into individual wave components.

Figure 31 shows the amplitude distributions along the plate of pressure perturbations at the frequency of 50 kHz and its first two harmonics induced by six cases of wall perturbations. The even higher harmonics are neglected in this figure because the corresponding pressure perturbation amplitudes are small. Specifically, Figs. 31(a) and 31(b) show the numerical results of wall oscillation and wall blowing-suction, respectively. Figures 31(c) to 31(f) show the results of temperature perturbations with the four different profile functions. It is clearly shown in all six figures that the pressure perturbations at the frequencies (f_n^*, $n \in \{1, 2, 3\}$) have similar properties, which indicates that different wall perturbations lead to the same boundary-layer instability (mode S). The receptivity of the hypersonic boundary layer to wall perturbations are independent of the specific type and profile function of perturbations. Downstream of the forcing region, the perturbation at the frequency of $f_2^* = 100$ kHz has the maximum amplitude. The figures also show that the pressure perturbations of wall blowing-suction is higher than that of wall oscillation. In turn, the pressure perturbations of wall oscillation is higher than that of temperature perturbations.

Figures 32, 33, and 34 compare the normalized pressure perturbation amplitudes of the cases 1, 2, and 3 at the frequencies of $f_1^* = 50$ kHz, $f_2^* = 100$ kHz, and $f_3^* = 150$ kHz, respectively. $|p_1\prime|_{nl}$, $|p_2\prime|_{nl}$, and $|p_3\prime|_{nl}$ are the normalized pressure perturbation amplitudes obtained by dividing the perturbation amplitudes with the corresponding dimensionless amplitudes listed in Table 3. Again, the similar properties of pressure perturbations indicate that the receptivity of the hypersonic boundary layer to wall perturbations are independent of the specific type of perturbations. These figures clearly show that the pressure perturbations of wall blowing-suction is higher than that of wall oscillation. In turn, the pressure perturbations of wall oscillation is higher than that of temperature perturbations. The boundary layer is much more sensitive to wall blowing-suction than to wall oscillation and temperature perturbation. These results are consistent with the theoretical and numerical analysis of Fedorov and Khokhlov[1].

Figures 35, 36, and 37 compare the dimensionless pressure perturbation amplitudes of the cases 3, 4, 5, and 6 at the frequencies of $f_1^* = 50$ kHz, $f_2^* = 100$ kHz, and $f_3^* = 150$ kHz, respectively. Again, the similar properties of pressure perturbations indicate that the receptivity of the hypersonic boundary layer to temperature perturbations are independent of the profile functions of perturbations. These figures also show that the perturbation amplitudes of case 4 are higher than those of the other cases. The perturbation amplitudes of cases 3 and 5 are approximately the same, and they are higher than those of case 6. Recall what have been discussed in Fig. 7, the integral energy introduced to the steady base flow has the maximum for case 4 and the minimum for case 6. It can be concluded that the amplitude of the pressure perturbation to temperature perturbation is proportional to the energy introduced to the steady base flow.

4.4 Receptivity to 3D stationary roughness elements

The receptivity of the Mach 5.92 boundary-layer flow to 3D stationary roughness elements are considered in this section. Three-dimensional steady base flow is extended from 2D base flow due to the fact that the flow field on a flat plate is independent of spanwise coordinate. Comparing with directly simulating the 3D steady base

flow, the extension from 2D flow to 3D flow greatly reduces the computation time. Stationary roughness elements modeled by Eqs. (32) and (34) are introduced on the flat plate in a region from $x_i^* = 3.3125$ mm and $x_e^* = 5.25$ mm, corresponding to $R = 207.51$ and $R = 261.25$, respectively. The subsequent responses of the hypersonic boundary layer are simulated by solving the three-dimensional Navier-Stokes equations with the fifth-order shock-fitting finite difference method. Specifically, a fifth-order upwind scheme is used to discretize the two inviscid flux derivatives of $\vec{F}_{1i}^*$ and $\vec{F}_{2i}^*$. A sixth-order central scheme is used to discretize the two viscous flux derivatives of $\vec{F}_{1v}^*$ and $\vec{F}_{2v}^*$. On the other hand, flux derivatives of $\vec{F}_{3i}^*$ and $\vec{F}_{3v}^*$ in spanwise direction are calculated by Fourier collocation method to achieve high accuracy. In the current paper, there is only one wave mode in spanwise direction. Therefore, four grid points in spanwise direction are enough for Fourier collocation method. The three-dimensional Navier-Stokes equations are solved by the parallel code of Dong and Zhong [33]. The computation load is uniformly distributed to the computer nodes.

To validate the accuracy of Fourier collocation method, one roughness element of constant height in spanwise direction is firstly considered. Adiabatic temperature condition is applied on the flat plate. For this special case, the parameters of the model are as follows:

$$\epsilon = 5.0 \times 10^{-7}, \beta^* = 0 \tag{48}$$

Figure 38 shows the velocity and temperature perturbation amplitudes induced by the roughness element of $\beta^* = 0$. The spanwise velocity perturbation, $w\prime$, is neglected in this figure. Since the steady base flow on a flat plate only has nonzero velocity components in streamwise and wall-normal directions, velocity perturbation in spanwise direction is equal to zero. Being different from the roughness models used by Collis & Lele [27] and Tumin [2], wall-normal velocity perturbation is induced in the current model because of the nonparallel nature of the numerically simulated flow. However, the amplitude of $v\prime$ is much smaller than that of $u\prime$ due to the property of boundary-layer flow. Unlike velocity perturbations, temperature perturbation is induced not only within the forcing region but downstream of the forcing region.

Since the roughness element has constant height in spanwise direction, the 3D flow field including the roughness element is independent of spanwise coordinate. A 2D flow field corresponding to a cross-section of 3D flow is simulated by solving the two-dimensional Navier-Stokes equations with a fifth-order shock-fitting method. Figure 39 compares the amplitude contours of pressure perturbations induced by the roughness element of $\beta^* = 0$ in 2D and 3D simulations. The good agreement between the solid contours of 2D simulation and the dashed contour of 3D simulation proves the accuracy of Fourier collocation method. Comparisons of amplitude distributions of pressure perturbations induced by the roughness element of $\beta^* = 0$ at two locations of $x^* = 3.31$ mm and $x^* = 5.54$ mm in 2D and 3D simulations ares shown in Fig. 40. Again, the good agreements between pressure perturbation amplitudes proves the accuracy of Fourier collocation method. Figure 40 also shows that the pressure perturbation propagates in wall-normal direction from upstream to downstream. Considering the displacement thickness of local boundary layer, the angle in the direction of pressure perturbation propagation is approximately equal to 9.6°, very close to the angle of Mach line. Therefore, the pressure perturbation outside the boundary layer propagates along the Mach lines, which is also shown in Fig. 39.

In order to check the transient growth phenomena, one roughness element of distributed height in spanwise direction is investigated. At first, adiabatic temperature condition is applied on the flat plate. For this case, the parameters of the model are as follows:

$$\epsilon = 1.0 \times 10^{-6}, \beta^* = 1.3 \times 10^4 \mathrm{m}^{-1} \tag{49}$$

The dimensional wave number can be non-dimensionalized by the local boundary layer thickness at the center of the roughness element as:

$$\beta = \beta^* L^* = 0.2247 \tag{50}$$

Figure 41 shows the contours of streamwise velocity perturbation on the plate induced by the 3D stationary roughness element of $\beta^* = 1.3 \times 10^4 \mathrm{m}^{-1}$. In this figure, four periods of the roughness element in spanwise direction are plotted. According to the roughness element model of Eq. (32), convex surface induces negative streamwise velocity whereas concave surface induces positive streamwise velocity. The contours in Fig. 41 are consistent with the profiles of roughness element in spanwise and streamwise directions.

Figure 42 plots the vector of $v\prime$ and $w\prime$ perturbations in the (y, z) plane at a location of $x^* = 5.4375$ mm, 0.1875 mm downstream of the trailing edge of the roughness element. It is clearly shown that there is a pair of counter rotating streamwise vortices induced by the roughness element. The vorticity is positive for the left-hand-side vortex and negative for the right-hand-side votex. Figures 43, 44, and 45 show the perturbation contours of

temperature, streamwise velocity, and streamwise vorticity at the same loaction of Fig. 42, respectively. In Fig. 43, the temperature increases in the wake region of convex surface roughness whereas it decreases in the wake region of concave surface roughness. On the contrary, there is a cold streak above the temperature-increased wake and a hot streak above the temperature-decreased wake. In Fig. 44, it is noticed that there are wake regions downstream of the distributed roughness. The speed of wake from convex surface roughness is slower than that from concave roughness. These results are similar to the theoretical analysis of Tumin [2], because the distributed roughness element in the current paper can also be regarded as a hump array in spanwise direction. Figure 45 clearly shows the pair of counter rotating vortices in the wake region. Above the wake region, there is another pair of counter rotating vortices at the location of $y^* = 5.6$ mm, which is stronger than the vortices in the wake region.

In compressible boundary layer, Tumin and Reshotko [49] used energy norm to measure the strength of transient growth. The energy norm is defined as

$$E_k = (\vec{q}, \vec{q})_2 = \int_0^\infty \vec{q}^T M \vec{q} dy \tag{51}$$

where the perturbation amplitude vector, $\vec{q}$, and the diagonal matrix, M, are expressed as

$$\vec{q} = (\hat{u}, \hat{v}, \hat{\rho}, \hat{T}, \hat{w})^T \tag{52}$$

$$M = diag[\rho, \rho, T/(\gamma \rho Me^2), \rho/(\gamma(\gamma-1)TMe^2), \rho] \tag{53}$$

In the current paper, the same energy norm is evaluated. The integral in Eq. (51) is numerical calculated across the boundary layer using a mid-point rule. Figure 46 shows energy norm distribution of transient growth along the adiabatic flat plate. It is found that the enery norm only has a small growth in the wake at the location of $x^* = 0.036$ m. The small energy norm may be caused by the small height of the roughness element. Figure 47 shows the distributions of streamwise and wall-normal velocity perturbations in wall-normal direction at the location of $x^* = 0.040$ mm. The strong oscillations of velocity perturbations outside the boundary layer ($50 < y^*/L^* < 120$) are related to the acoustic waves propagating along the Mach lines. Profiles of the two vecolity perturbations in the boundary layer indicate the transient growth. However, the transient growth is quite low in this case, which is consitent with the small energy norm in Fig. 46.

When isothermal temperature condition is applied to the plate with the same distributed roughness element defined in Eq. (49), similar results can be achieved. Counter rotating streamwise vortices are excited by wall roughness. And the temperature increases in the wake region of convex surface roughness whereas it decreases in the wake region of concave surface roughness. Furthermore, the speed of wake from convex surface roughness is slower than that from concave roughness. Figure 48 shows streamwise vorticity distributions along the adiabatic and isothermal flat plates at $x^* = 5.4375$ mm. Despite the similar profiles of the streamwise vorticity distributions, the streamwise vorticity excited on adiabatic plate is stronger than that excited on isothermal plate, which indicates that the roughness element on adiabatic flat plate is more efficient in the excitation of transient growth. Figure 49 shows energy norm distributions of transient growth along the adiabatic and isothermal flat plates. It is noticed that the enery norm for the roughness element on isothermal flat plate also has a small growth in the wake at the location of $x^* = 0.036$ m. However, the energy norm at that location for isothermal flat plate is lower than that for adiabatic flat plate, which indicates that the roughness element on adiabatic flat plate is more efficient in the excitation of transient growth.

5 Summary

The objective of this paper is to numerically investigate the receptivity of a Mach 5.92 flat plate boundary layer to two and three-dimensional wall perturbations. The 2D steady base flow is simulated by solving two-dimensional compressible Navier-Stokes equations with a combination of a fifth-order shock-fitting finite difference method and a second-order TVD scheme. Three-dimensional steady base flow is extended from 2D base flow due to the fact that the flow field on a flat plate is independent of spanwise coordinate. The characteristics of boundary-layer wave modes are identified and evaluated by comparing the results of LST and numerical simulations. Two-dimensional wall perturbations of six cases are introduced to 2D steady base flow by a forcing slot located on the flat plate. In order to investigate the transient growth phenomena, small-scale stationary three-dimensional roughness elements are introduced on the flat plate. The surface roughness is periodic in spanwise direction. Effect of thermal flat plate boundary conditions on the receptivity process is considered by comparing numerical simulations on adiabatic and isothermal flat plates, respectively.

The main conclusions of the current study are:

- All six cases of 2D wall perturbations eventually result in the same type of instability wave (mode S) in the boundary layer, which indicates that receptivity of the hypersonic boundary layer to 2D wall perturbations is independent of the specific type and profile of perturbations.
- The hypersonic boundary-layer flow is more sensitive to blowing-suction than to wall oscillation and temperature perturbations, which is consistent with the theoretical and numerical analysis of Fedorov and Khokhlov [1]. The receptivity of the hypersonic boundary layer to temperature perturbation is proportional to the energy introduced to the steady base flow.
- Counter rotating streamwise vortices are excited by stationary roughness element. The temperature increases in the wake region of convex surface roughness whereas it decreases in the wake region of concave surface roughness. Furthermore, the speed of wake from convex surface roughness is slower than that from concave roughness. All these results are consistent with those of Tumin's theoretical analysis [2].
- The roughness element on adiabatic flat plate is more efficient in the excitations of streamwise vortices and transient growth.

Receptivity of the hypersonic boundary layer to more cases of 3D stationary roughness elements and non-stationary roughness elements will be carried out to further investigate the transient growth phenomena.

Acknowledgments

This work was sponsored by the Air Force Office of Scientific Research, USAF, under AFOSR Grant #FA9550-04-1-0029, monitored by Dr. John Schmisseur. This research was also supported by the AAP program of advanced computing resources supported by NSF. The three-dimensional computations are performed in part on the IA-64 cluster at the San Diego Supercomputing Center. The views and conclusions contained herein are those of the authors and should not be interpreted as necessarily representing the official policies or endorsements either expressed or implied, of the Air Force Office of Scientific Research or the U.S. Government.

References

[1] A. V. Fedorov and A. P. Khokhlov. Receptivity of Hypersonic Boundary Layer to Wall Disturbances. *Theoretical and Computational Fluid Dynamics*, Vol.15, pp.231-254, 2002.

[2] A. Tumin. Receptivity of compressible boundary layers to three-dimensional wall perturbations. *AIAA paper 2006-1110*, January 2006.

[3] M. E. Goldstein and L. S. Hultgren. Boundary-layer receptivity to long-wave free-stream disturbances. *Annual Review of Fluid Mechanics*, Vol.21, pp.137-166, 1989.

[4] L. M. Mack. Linear Stability Theory and the Problem of Supersonic Boundary-Layer Transition. *AIAA Journal*, Vol.13, No.3, pp.278-289, 1975.

[5] P. Balakumar, P. Hall, and M. R. Malik. On the receptivity and non-parallel stability of travelling disturbances in rotating disk flow. *ICASE Report*, No.90-89, 1990.

[6] F. P. Bertolotti. Vortex generation and wave-vortex interaction over a concave plate with roughness and suction. *ICASE Report*, No.93-101, 1993.

[7] M. Choudhari. Roughness-induced generation of crossflow vortices in three-dimensional boundary layers. *Theoretical and Computational Fluid Dynamics*, Vol.6, pp.1-30, 1994.

[8] A. Hanifi, P. J. Schmid, and D. S. Henningson. Transient growth in compressible boundary layer flow. *Physics of Fluids*, Vol.8, No.3, pp.826-837, 1996.

[9] P. Andersson, M. Berggren, and D. S. Henningson. Optimal Disturbances and Bypass Transition in Boundary Layers. *Physics of Fluids*, Vol.11, No.1, pp.134-150, 1999.

[10] T. Herbert. On the stability of 3D boundary layers. *AIAA paper 1997-1961*, June 1997.

[11] E. Reshotko. Transient growth: A factor in bypass transition. *Physics of Fluids*, Vol.13, No.5, pp.1067-1075, 2001.

[12] E. Reshotko and A. Tumin. Role of transient growth in roughness-induced transition. *AIAA Journal*, Vol.42, No.4, pp.766-770, 2004.

[13] E. Forgoston and A. Tumin. Three-dimensional wave packet in a hypersonic boundary layer. *AIAA paper 2005-0099*, January 2005.

[14] J. M. Kendall. Wind Tunnel Experiments Relating to Supersonic and Hypersonic Boundary-Layer Transition. *AIAA Journal*, Vol.13, No.3, pp.290–299, 1975.

[15] A. A. Maslov and N. V. Seminov. Excitation of natural oscillations in a boundary layer by an external acoustic field. *Fluid Dynamics (Historical Archive)*, Vol.21, pp.400-404, 1986.

[16] A. A. Maslov, A. N. Shiplyuk, A. Sidorenko, and D. Arnal. Leading-edge receptivity of a hypersonic boundary layer on a flat plate. *Jounral of Fluid Mechanics*, Vol.426, pp.73-94, 2001.

[17] M. Gaster, C. E. Grosch, and T. L. Jackson. The velocity field created by a shallow bump in a boundary layer. *Physics of Fluids*, Vol.6, No.9, pp.3079-3085, 1994.

[18] A. A. Bakchinov, G. R. Grek, B. G. B. Klingmann, and V. V. Kozlov. Transition experiments in boundary layer with embedded streamwise vortices. *Physics of Fluids*, Vol.7, No.4, pp.820-832, 1995.

[19] E. B. White. Transient growth of stationary disturbances in a flat plate boundary layer. *Physics of Fluids*, Vol.14, No.12, pp.4429-4439, 2002.

[20] E. B. White and F. G. Ergin. Receptivity and transient growth of roughness-induced disturbances. *AIAA paper 2003-4243*, June 2002.

[21] J. H. M. Fransson and L. Brandt. Experimental and theoretical investigation of the nonmodal growth of steady streaks in a flat plate boundary layer. *Physics of Fluids*, Vol.16, No.10, pp.3627-3638, 2004.

[22] E. B. White, J. M. Rice, and F. G. Ergin. Receptivity of stationary transient disturbances to surface roughness. *Physics of Fluids*, Vol.17, No.6, Paper No.064109, 2005.

[23] T. Kawamura, H. Takami, and K. Kuwahara. Computation of high Reynolds number flow around a circular cylinder with surface roughness. *Fluid Dynamics Research*, Vol.1, pp.145-162, 1986.

[24] R. D. Joslin and C. E. Grosch. Growth characteristics downstream of a shallow bump: Computation and experiment. *Physics of Fluids*, Vol.7, No.12, pp.3042-3047, 1995.

[25] A. Bottaro and A. Zebib. Görtler vortices promoted by wall roughness. *Fluid Dynamics Research*, Vol.19, pp.343-362, 1997.

[26] C. Stemmer, M. J. Kloker, and S. Wagner. DNS of harmonic point source disturbances in an airfoil boundary layer flow. *AIAA paper 1998-2346*, June 1998.

[27] S. S. Collis and S. K. Lele. Receptivity to surface roughness near a swept leading edge. *Journal of Fluid Mechanics*, Vol.380, pp.141-168, 1999.

[28] M. R. Malik, R. S. Lin, and R. Sengupta. Computation of Hypersonic Boundary-Layer Response to External Disturbances. *AIAA Paper 1999-0411*, January 1999.

[29] X. Zhong. Leading-Edge Receptivity to Free Stream Disturbance Wave for Hypersonic Flow Over A Parabola. *Journal of Fluid Mechanics*, Vol.441, pp.315-367, 2001.

[30] Y. Ma and X. Zhong. Receptivity of a supersonic boundary layer over a flat plate. Part 1:Wave Structures and Interactions. *Journal of Fluid Mechanics*, Vol.488, pp.31-78, 2003.

[31] Y. Ma and X. Zhong. Receptivity of a supersonic boundary layer over a flat plate. Part 2:Receptivity to Freestream Sound. *Journal of Fluid Mechanics*, Vol.488, pp.79-121, 2003.

[32] Y. Ma and X. Zhong. Receptivity of a supersonic boundary layer over a flat plate. Part 3. Effects of different types of free-stream disturbances. *Journal of Fluid Mechanics*, Vol.532, pp.63-109, 2005.

[33] H. Dong and X. Zhong. Numerical simulations of transient growth in a Mach 15 boundary layer over a blunt leading edge. *AIAA paper 2003-1266*, January 2003.

[34] I. V. Egorov, A. V. Fedorov, and V. G. Soudakov. Direct Numerical Simulation of Unstable Disturbances in Supersonic Boundary Layer. *AIAA paper 2004-0588*, January 2004.

[35] P. Fischer and M. Choudhari. Numerical simulation of roughness-induced transient growth in a laminar boundary layer. *AIAA paper 2004-2539*, June 2004.

[36] M. Choudhari and P. Fischer. Roughness-induced transient growth. *AIAA paper 2005-4765*, June 2005.

[37] Y. Ma and X. Zhong. Receptivity to Freestream Disturbances of Mach 8 Flow over A Sharp Wedge. *AIAA paper 2003-0788*, 2003.

[38] X. Wang and X. Zhong. Receptivity of a supersonic boundary layer over a sharp wedge to wall blowing/suction. *AIAA paper 2004-0254*, January 2004.

[39] X. Wang and X. Zhong. Receptivity of A Mach 8.0 Flow over A Sharp Wedge to Wall Blowing-Suction. *AIAA paper 2005-5025*, June 2005.

[40] A. Tumin, X. Wang, and X. Zhong. Direct Numerical Simulation of Receptivity in a Hypersonic Boundary Layer: Validation. *AIAA paper 2006-1108*, January 2006.

[41] X. Zhong and Y. Ma. Boundary-layer receptivity of Mach 7.99 flow over a blunt cone to free-stream acoustic waves. *Journal of Fluid Mechanics*, Vol.556, pp.55-103, 2006.

[42] X. Zhong. High-Order Finite-Difference Schemes for Numerical Simulation of Hypersonic Boundary-Layer Transition. *Journal of Computational Physics*, Vol.144, pp. 662-709, 1998.

[43] X. Zhong. Additive Semi-Implicit Runge-Kutta Schemes for Computing High-Speed Nonequilibrium Reactive Flows. *Journal of Computational Physics*, Vol.128, pp.19-31, 1996.

[44] X. Zhong and T. Lee. Nonequilibrium real-gas effects on disturbance/bow shock interaction in hypersonic flow past a cylinder. *AIAA paper 1996-1856*, January 1996.

[45] X. Zhong. Receptivity of Mach 6 flow over a flared cone to freestream disturbance. *AIAA paper 2004-0253*, January 2004.

[46] Y. Ma and X. Zhong. Receptivity to Freestream Disturbances of Mach 4.5 Flow over A Flat Plate. *AIAA Paper 2002-0140*, January 2002.

[47] X. Wang and X. Zhong. Numerical Simulation and Experiment Comparison of Leading-Edge Receptivity of A Mach 5.92 Boundary Layer. *AIAA paper 2006-1107*, January 2006.

[48] M. R. Malik. Numerical methods for hypersonic boundary layer stability. *Journal of Computational Physics*, Vol.86, pp.376-413, 1990.

[49] A. Tumin and E. Reshotko. Spatial Theory of Optimal Disturbances in Boundary Layers. *Physics of Fluids*, Vol.13, No.7, 2001.

Table 1: Locations of the Branch I and Branch II neutral points, x^*_{In} and x^*_{IIn}, for the base frequency and its first 14 harmonics

n	$f^*(kHz)$	$F_n \times 10^6$	x^*_I (m)	x^*_{II} (m)
1	50	26.51479	6.78977^{-3}	3.38487
2	100	53.02959	1.69744^{-3}	0.84622
3	150	79.54438	7.54418^{-4}	0.37610
4	200	106.05918	4.24360^{-4}	0.21155
5	250	132.57397	2.71591^{-4}	0.13539
6	300	159.08876	1.88604^{-4}	0.09402
7	350	185.60356	1.38567^{-4}	0.06908
8	400	212.11835	1.06090^{-4}	0.05289
9	450	238.63315	8.38243^{-5}	0.04179
10	500	265.14794	6.78976^{-5}	0.03385
11	550	291.66274	5.61138^{-5}	0.02797
12	600	318.17753	4.71511^{-5}	0.02351
13	650	344.69233	4.01761^{-5}	0.02003
14	700	371.20712	3.46416^{-5}	0.01727
15	750	397.72191	3.01767^{-5}	0.01504

Table 2: Types and profile functions of two-dimensional wall perturbations for the six cases considered in the current study

n	(Q_u,Q_v,Q_T)	Profile
1	$(1,0,0)$	$F(l_1)$ as in Eq. (19)
2	$(0,1,0)$	$G(l_2)$ as in Eq. (21)
3	$(0,0,1)$	$H_1(l_3)$ as in Eq. (23)
4	$(0,0,1)$	$H_2(l_3)$ as in Eq. (24)
5	$(0,0,1)$	$H_3(l_3)$ as in Eq. (26)
6	$(0,0,1)$	$H_4(l_3)$ as in Eq. (28)

Table 3: Dimensional and dimensionless amplitudes of two-dimensional wall perturbations for the six cases considered in the current study

n	Amplitude	Dimensionless amplitude
1	$8.885 \times 10^{-2} m/s$	1.073×10^{-4}
2	4.401×10^{-4} kg/m$^2 s$	1.0×10^{-5}
3	4.869×10^{-2} K	1.0×10^{-3}
4	4.869×10^{-2} K	1.0×10^{-3}
5	4.869×10^{-2} K	1.0×10^{-3}
6	4.869×10^{-2} K	1.0×10^{-3}

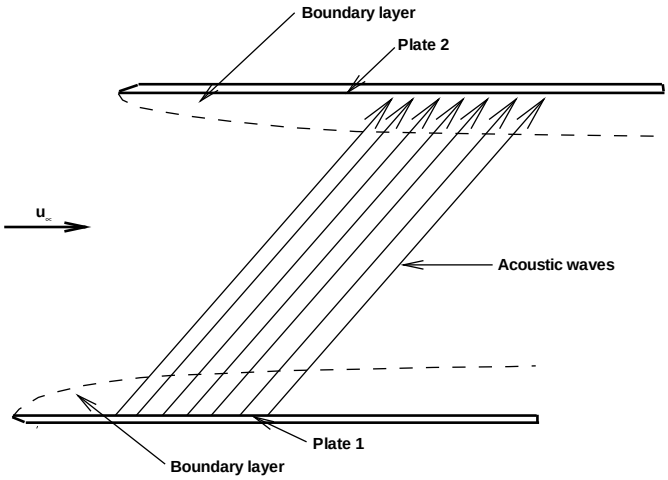

Figure 1: A schematic of the receptivity experiment setup by Maslov and Seminov[15].

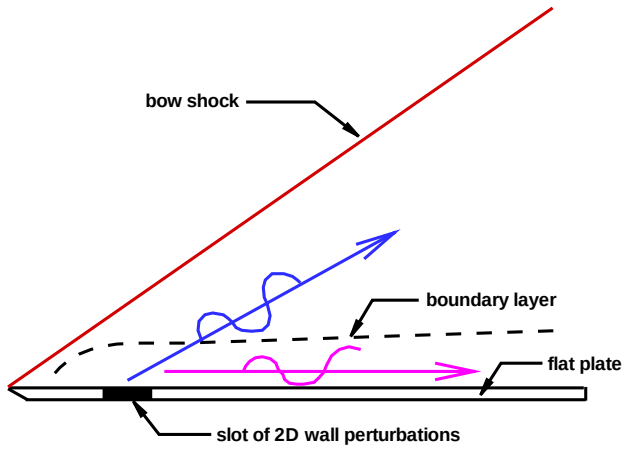

Figure 2: A schematic of the receptivity of the Mach 5.92 flow to two-dimensional wall perturbations.

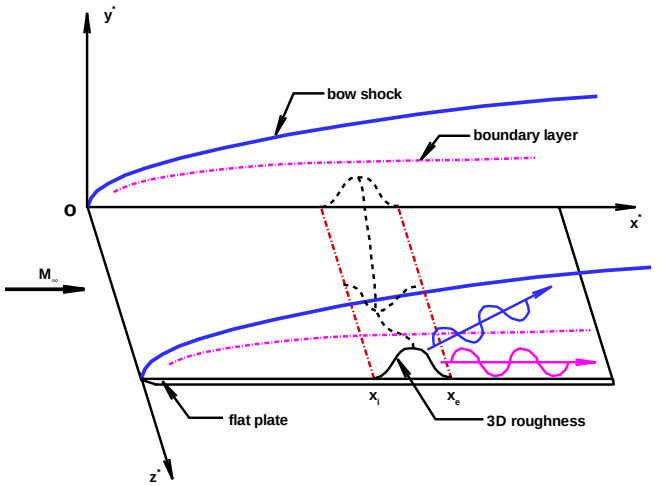

Figure 3: A schematic of the receptivity of the Mach 5.92 flow to three-dimensional roughness elements.

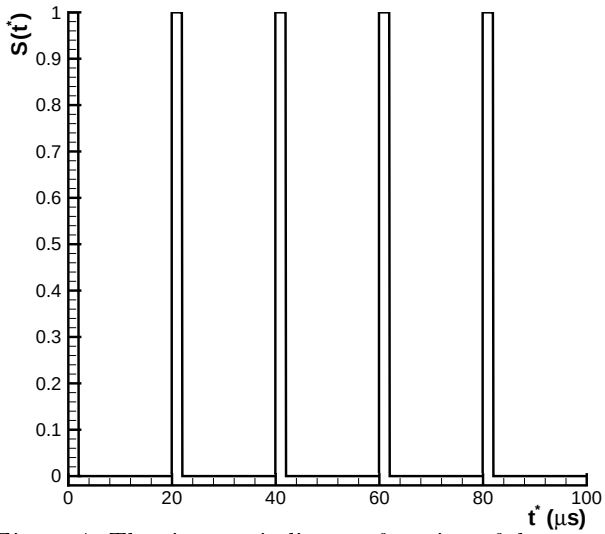

Figure 4: The time-periodic step function of the perturbation model in the current study ($S(t^*)$ vs time (t^*).

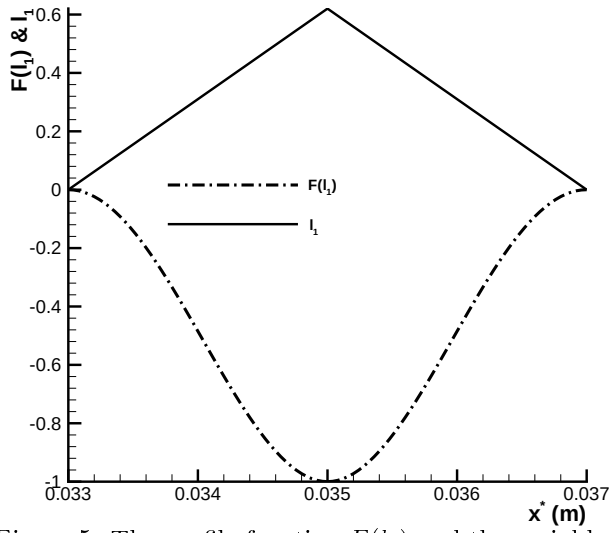

Figure 5: The profile function $F(l_1)$ and the variable l_1 within the forcing region for the case of wall oscillation.

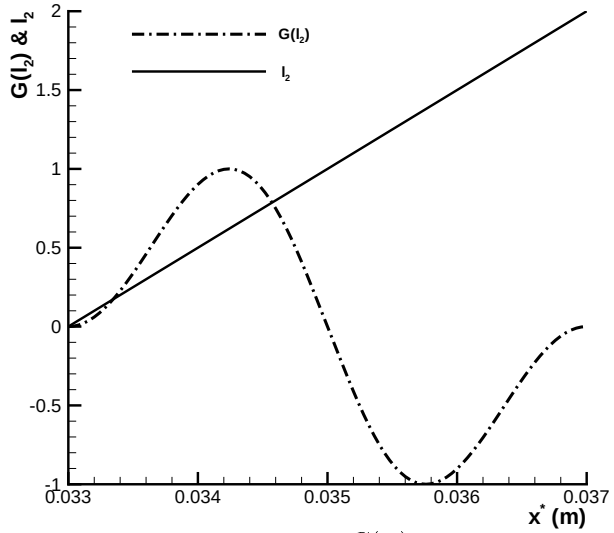

Figure 6: The profile function $G(l_2)$ and the variable l_2 within the forcing region for the case of wall blowing-suction.

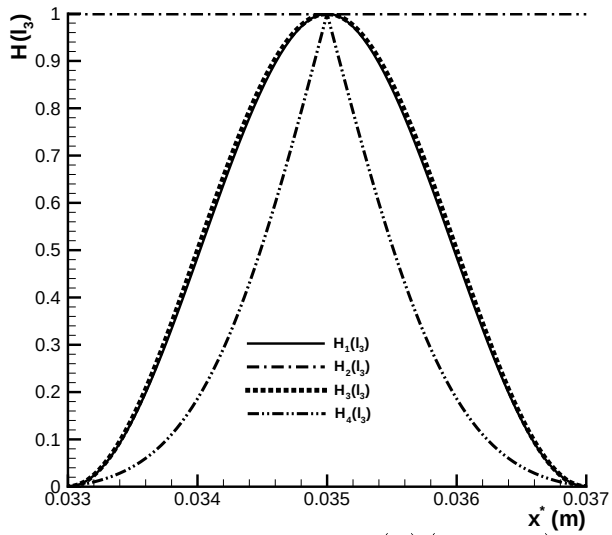

Figure 7: The profile functions $H_i(l_3)$ $(i = 1 \sim 4)$ within the forcing region for the four cases of temperature perturbations.

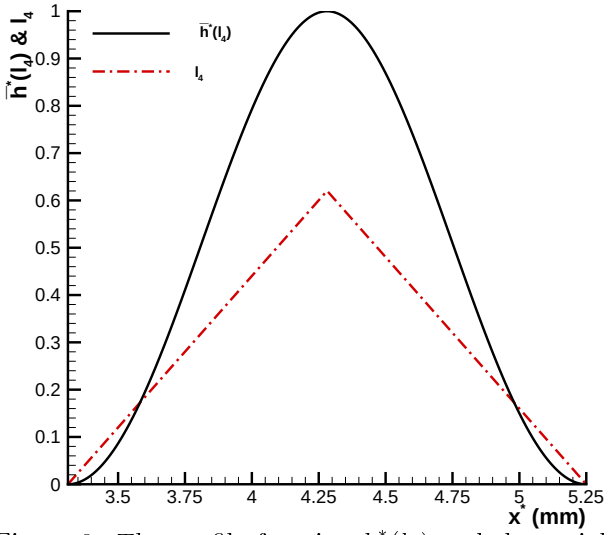

Figure 8: The profile function $\hbar^*(l_4)$ and the variable l_4 of the roughness element in streamwise direction.

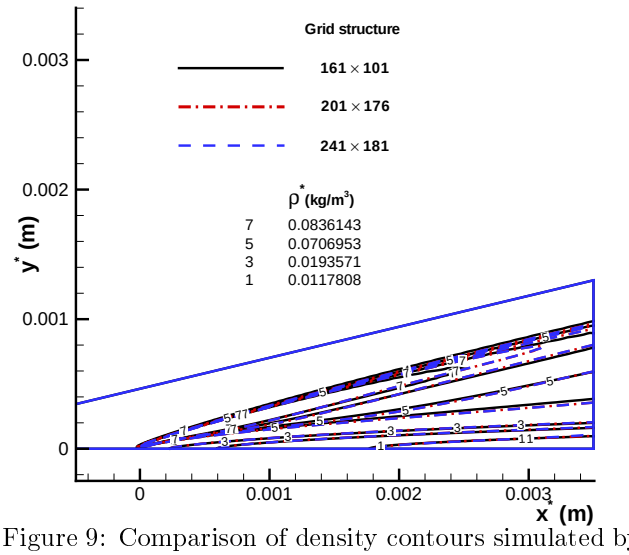

Figure 9: Comparison of density contours simulated by TVD scheme based on the three sets of grid structures.

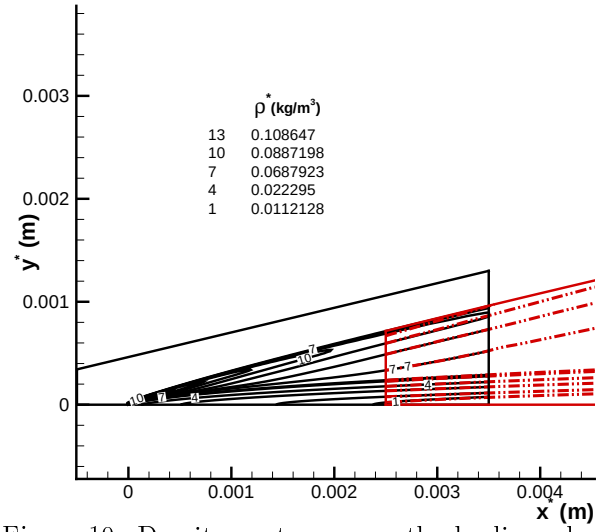

Figure 10: Density contours near the leading edge for the steady base flows over the plate obtained by TVD scheme and shock-fitting method.

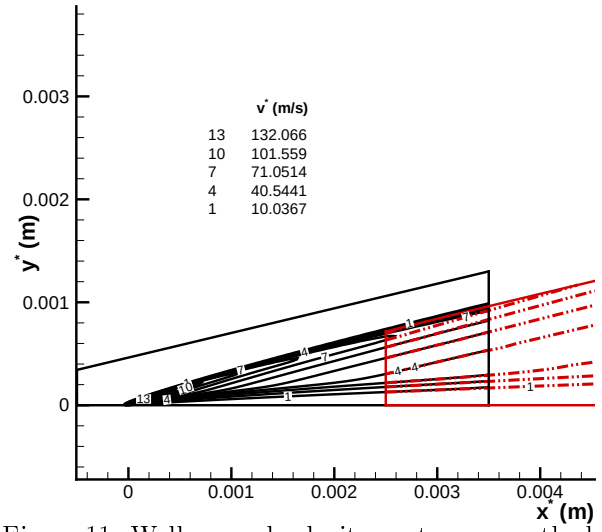

Figure 11: Wall-normal velocity contours near the leading edge for the steady base flows over the plate obtained by TVD scheme and shock-fitting method.

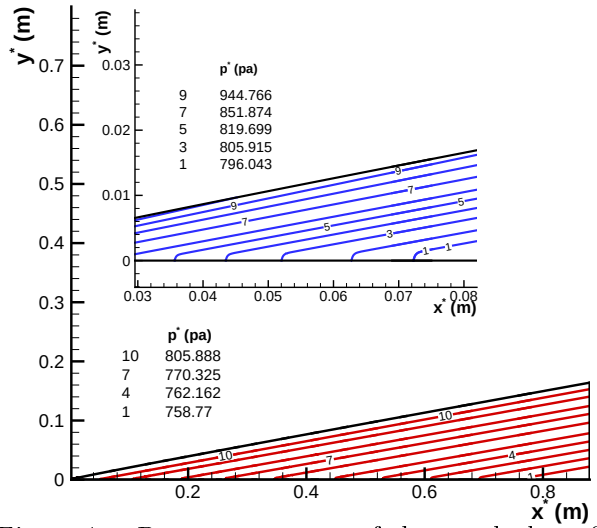

Figure 12: Pressure contours of the steady base flow simulated by the fifth-order shock-fitting method.

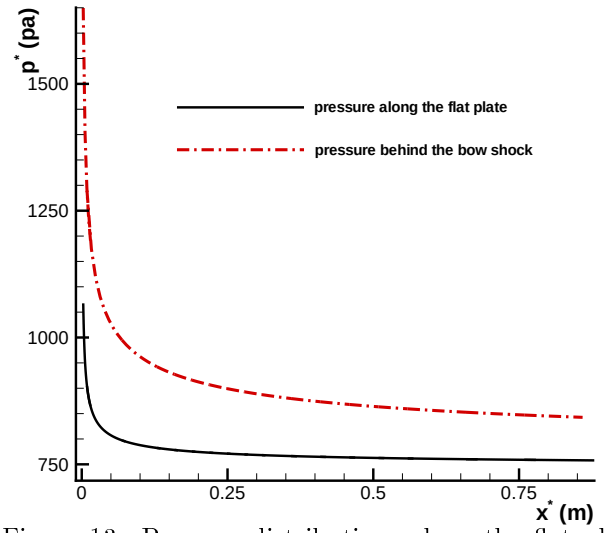

Figure 13: Pressure distributions along the flat plate and behind the shock of the steady base flow.

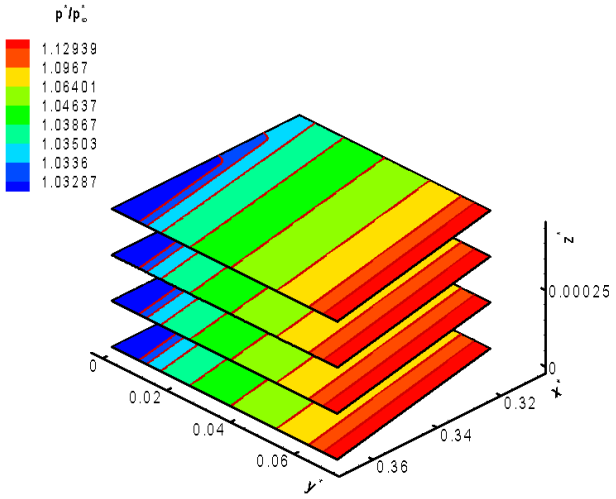

Figure 14: Pressure contours in spanwise cross-sections of 3D base flow extended from 2D base flow.

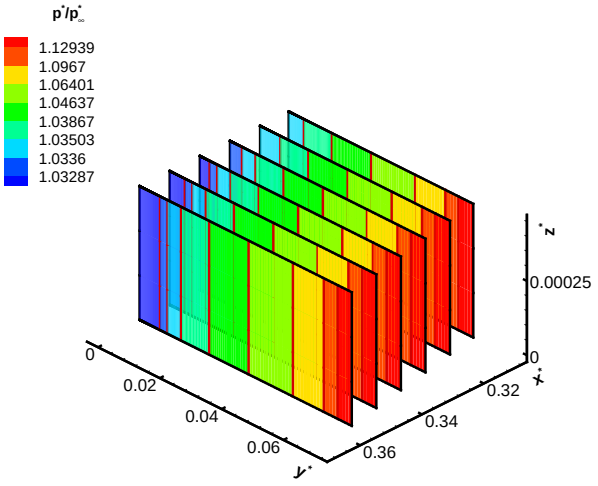

Figure 15: Pressure contours in streamwise cross-sections of 3D base flow extended from 2D base flow.

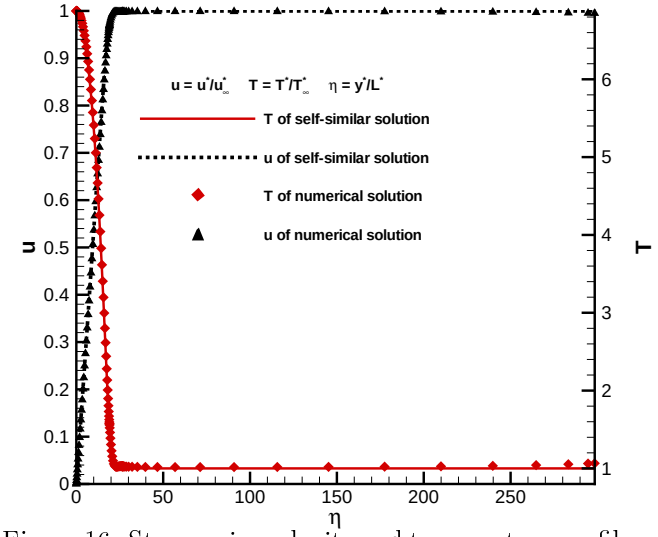

Figure 16: Streamwise velocity and temperature profiles in wall-normal direction at location $x^* = 0.159$ m.

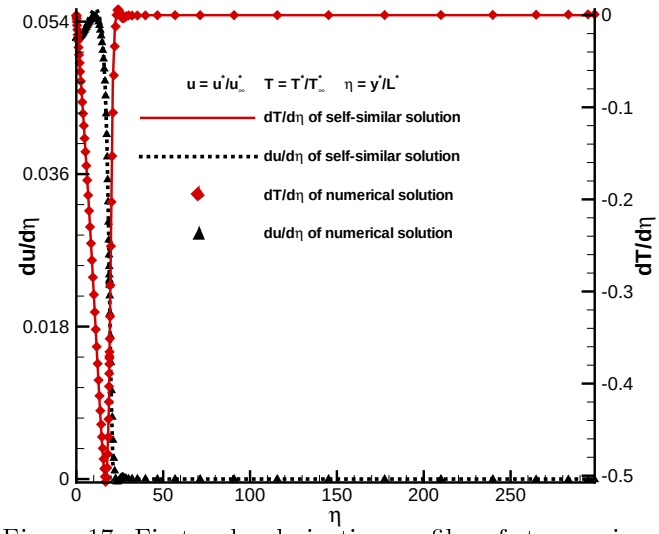

Figure 17: First-order derivative profiles of streamwise velocity and temperature at location $x^* = 0.159$ m.

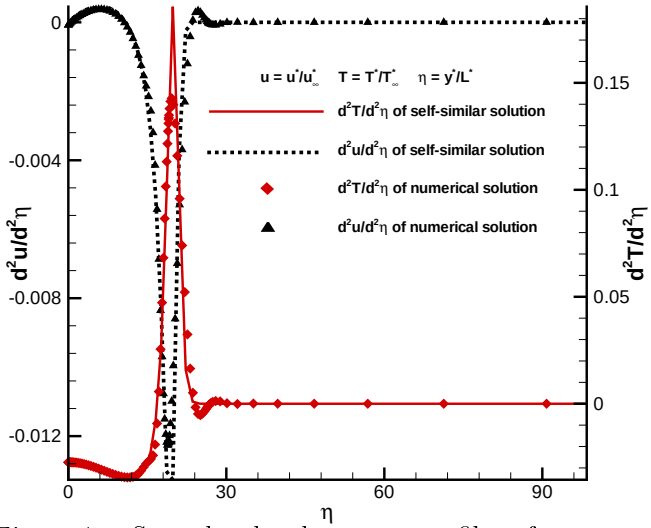

Figure 18: Second-order derivative profiles of streamwise velocity and temperature at location $x^* = 0.159$ m.

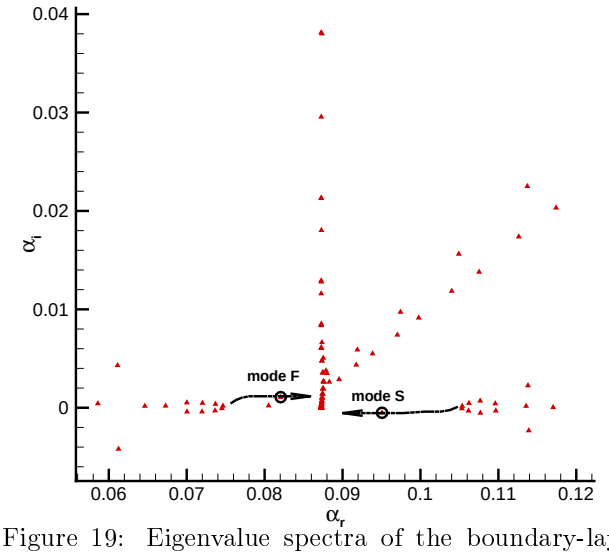

Figure 19: Eigenvalue spectra of the boundary-layer modes for a case at the frequency of $f^* = 100$ kHz at $x^* = 0.189$ m.

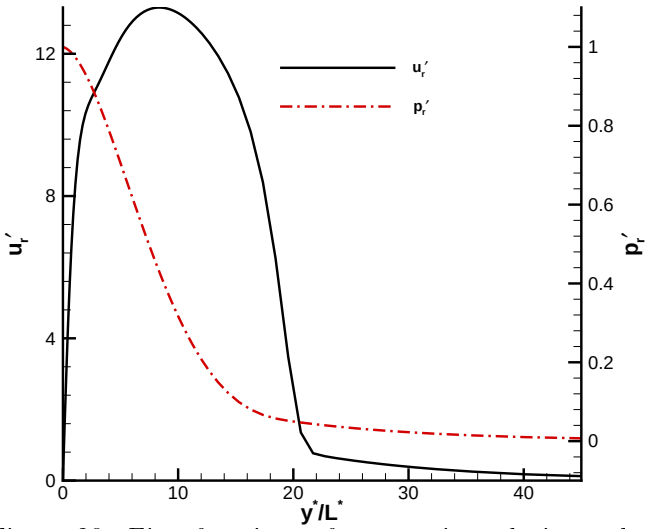

Figure 20: Eigenfunctions of streamwise velocity and pressure fluctuations of mode F at $x^* = 0.189$ m.

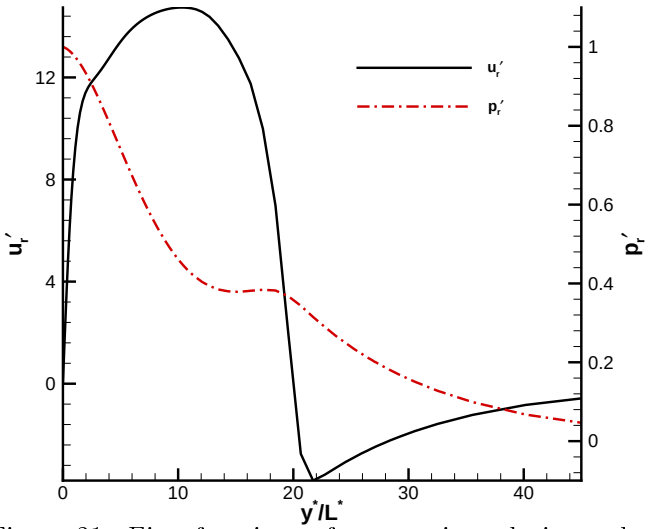

Figure 21: Eigenfunctions of streamwise velocity and pressure fluctuations of mode S at $x^* = 0.189$ m.

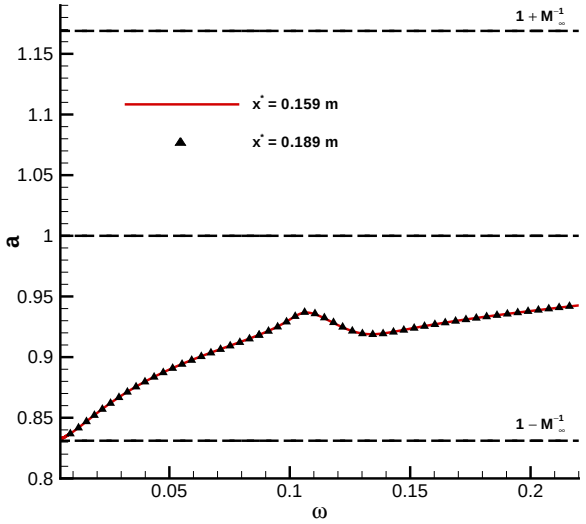

Figure 22: Distributions of dimensionless phase velocities of mode S at two locations versus ω.

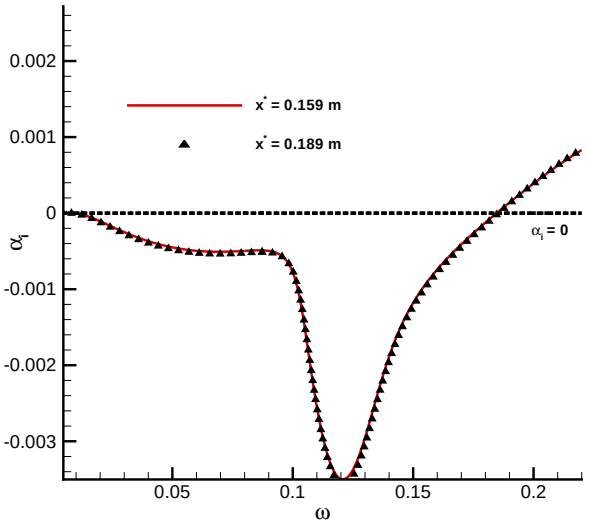

Figure 23: Distributions of growth rates of mode S at the two locations versus ω.

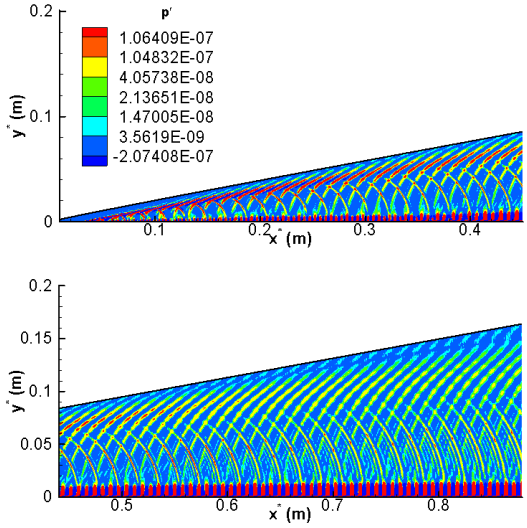

Figure 24: Contours of the instantaneous pressure perturbation induced by 2D wall oscillation in case 1.

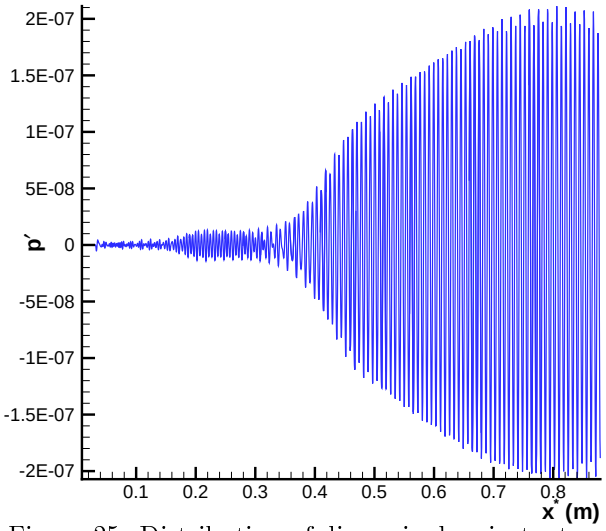

Figure 25: Distribution of dimensionless instantaneous pressure perturbation along the flat plate in case 1.

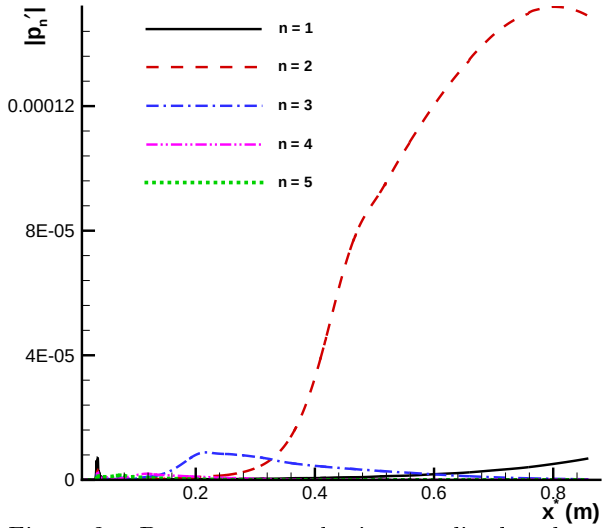

Figure 26: Pressure perturbation amplitudes along the wall at frequencies from f_1^* to f_5^* in case 1.

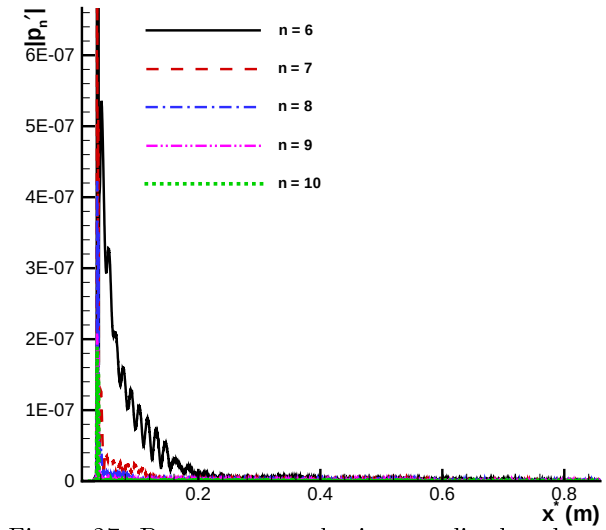

Figure 27: Pressure perturbation amplitudes along the wall at frequencies from f_6^* to f_{10}^* in case 1.

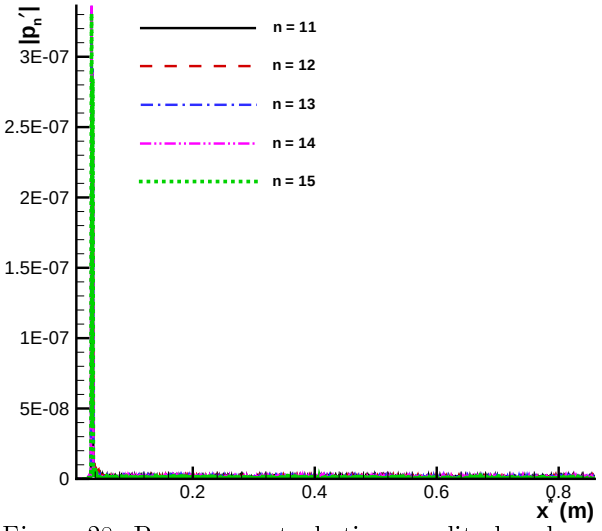

Figure 28: Pressure perturbation amplitudes along the wall at frequencies from f_{11}^* to f_{15}^* in case 1.

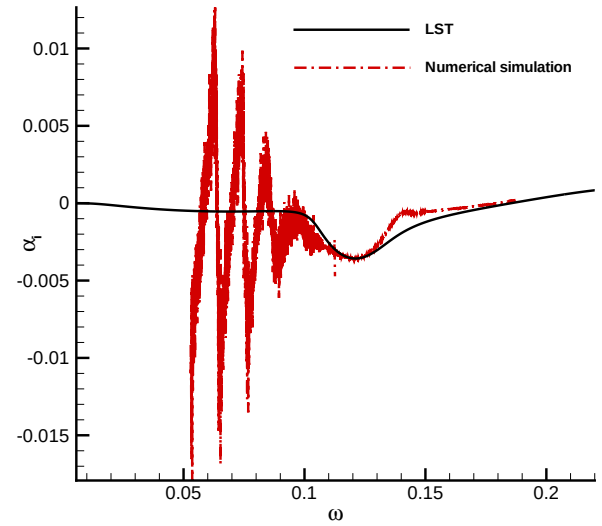

Figure 29: Comparison of numerical growth rate and LST growth rate of the perturbation at frequency f_2^*.

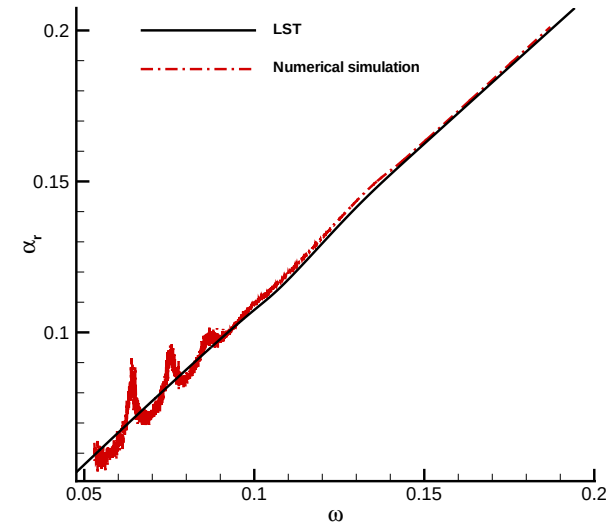

Figure 30: Comparison of numerical wave number and LST wave number of the perturbation at frequency f_2^*.

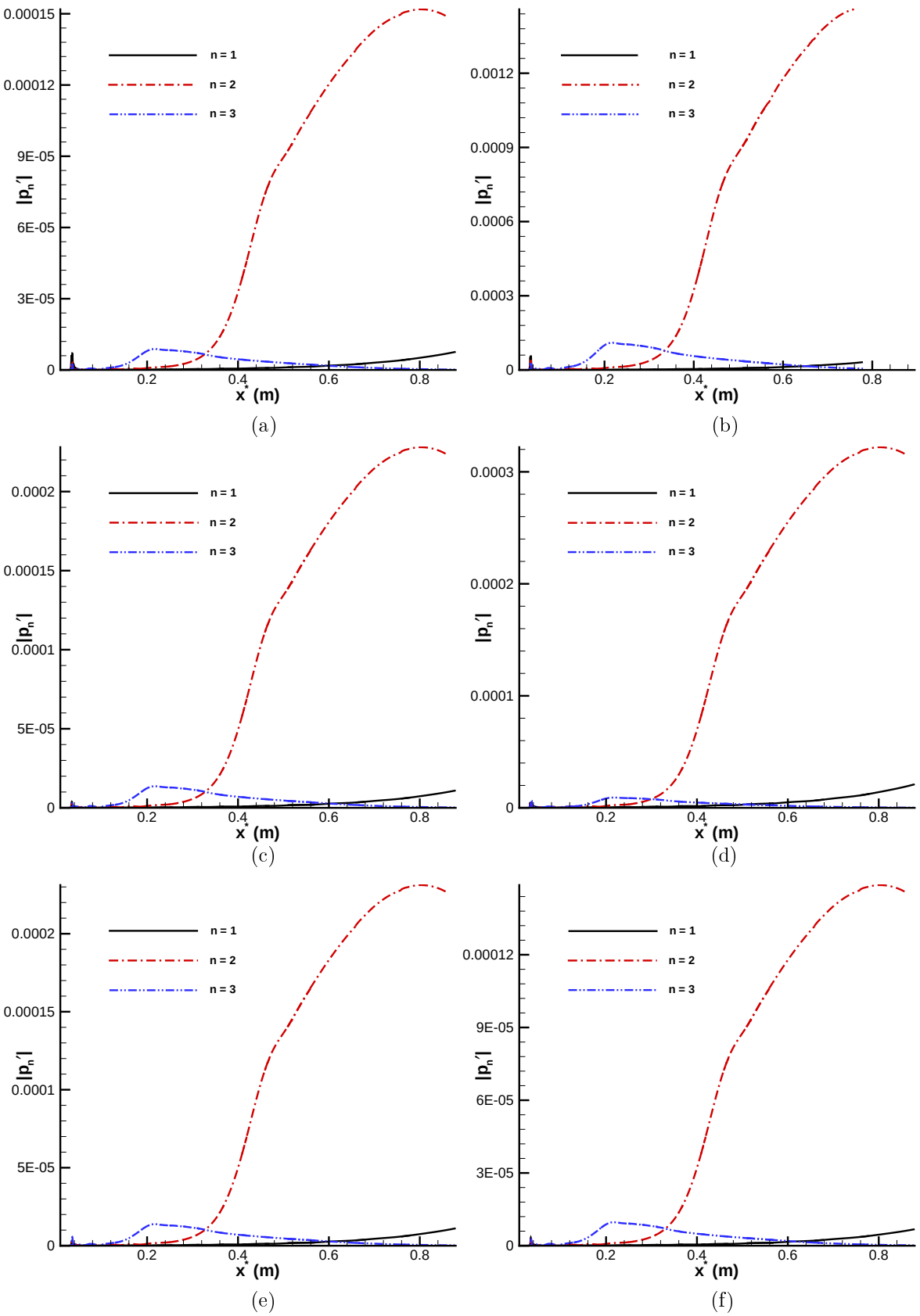

Figure 31: Amplitude distributions along the plate of pressure perturbations at the frequency 50 kHz and its first two harmonics induced by six cases of wall perturbations: (a) case 1; (b) case 2; (c) case 3; (d) case 4; (e) case 5; (f) case 6.

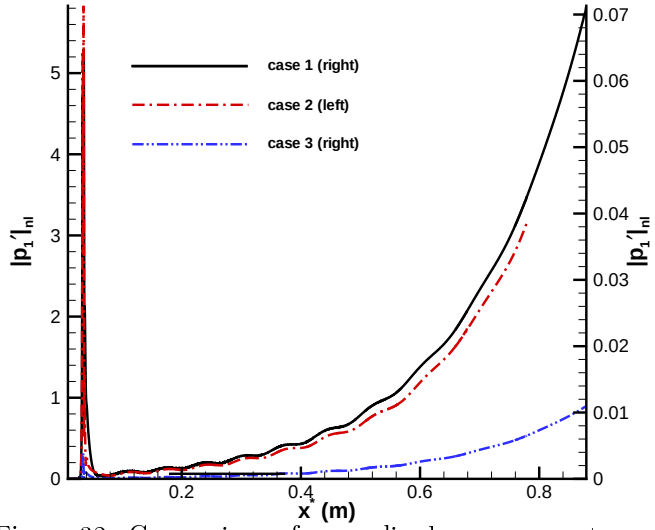

Figure 32: Comparison of normalized pressure perturbation amplitudes of the cases 1, 2, and 3 ($f_1^* = 50$ kHz).

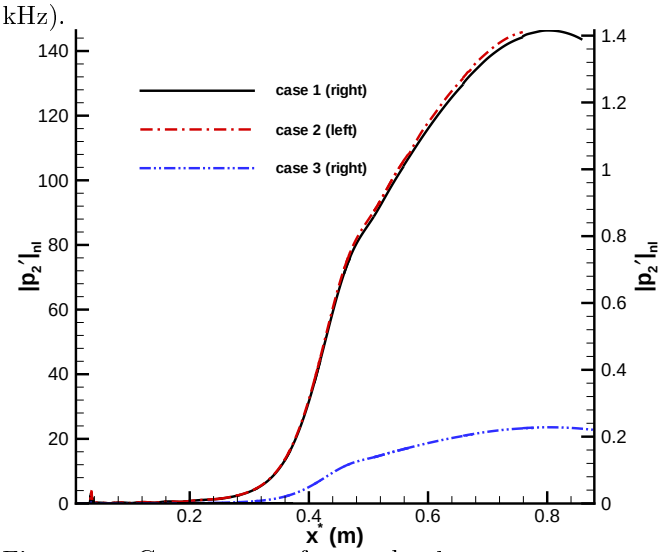

Figure 33: Comparison of normalized pressure perturbation amplitudes of the cases 1, 2, and 3 ($f_2^* = 100$ kHz).

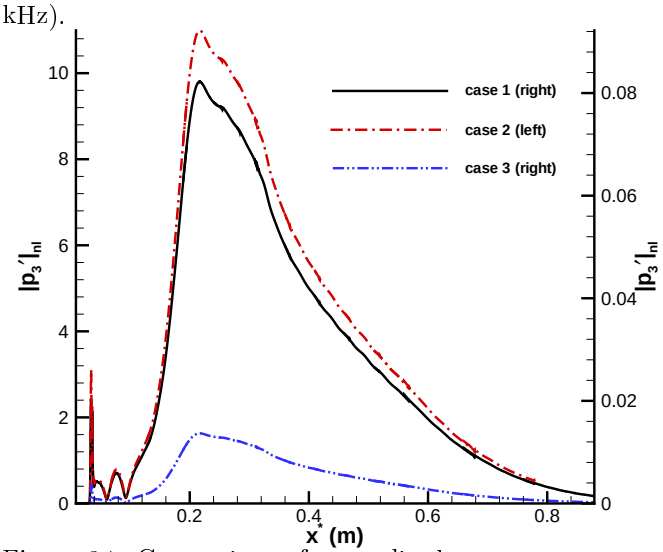

Figure 34: Comparison of normalized pressure perturbation amplitudes of the cases 1, 2, and 3 ($f_3^* = 150$ kHz).

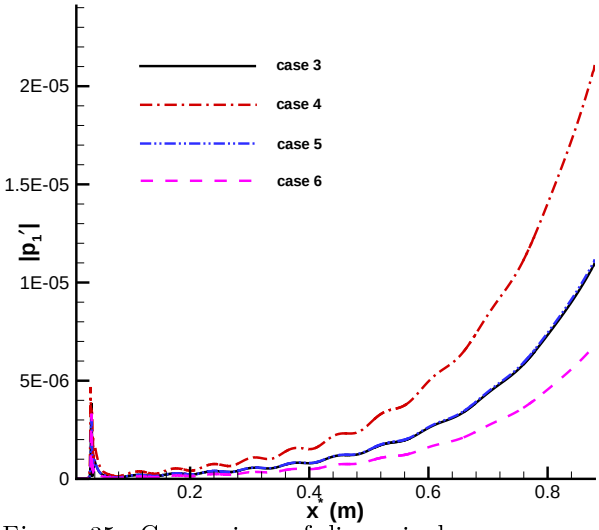

Figure 35: Comparison of dimensionless pressure perturbation amplitudes of the cases 3, 4, 5, and 6 ($f_1^* = 50$ kHz).

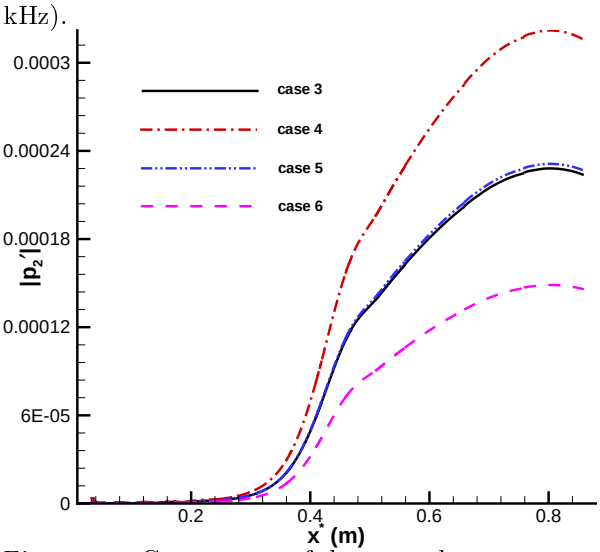

Figure 36: Comparison of dimensionless pressure perturbation amplitudes of the cases 3, 4, 5, and 6 ($f_2^* = 100$ kHz).

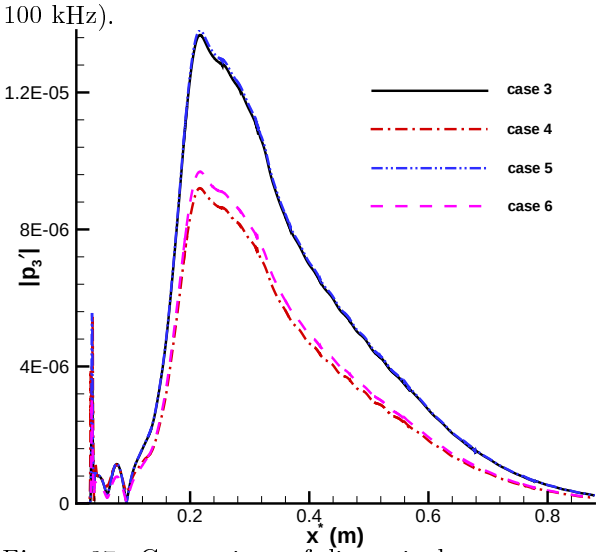

Figure 37: Comparison of dimensionless pressure perturbation amplitudes of the cases 3, 4, 5, and 6 ($f_3^* = 150$ kHz).

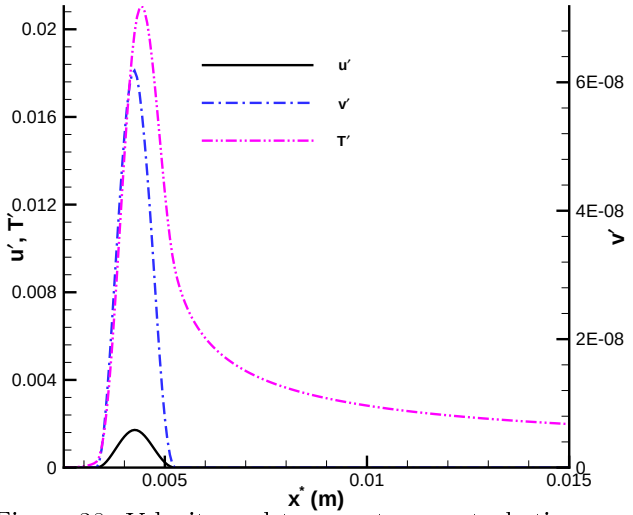

Figure 38: Velocity and temperature perturbation amplitudes on the plate induced by the roughness element of $\beta^* = 0$.

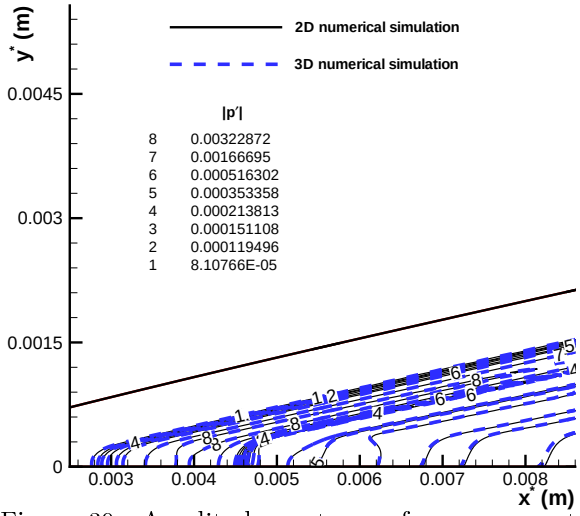

Figure 39: Amplitude contours of pressure perturbations induced by the roughness element of $\beta^* = 0$ in 2D and 3D simulations.

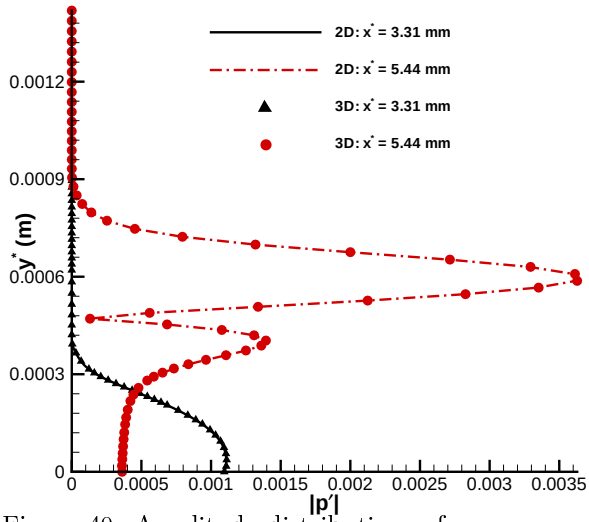

Figure 40: Amplitude distributions of pressure perturbations induced by the roughness element of $\beta^* = 0$ at two locations in 2D and 3D simulations.

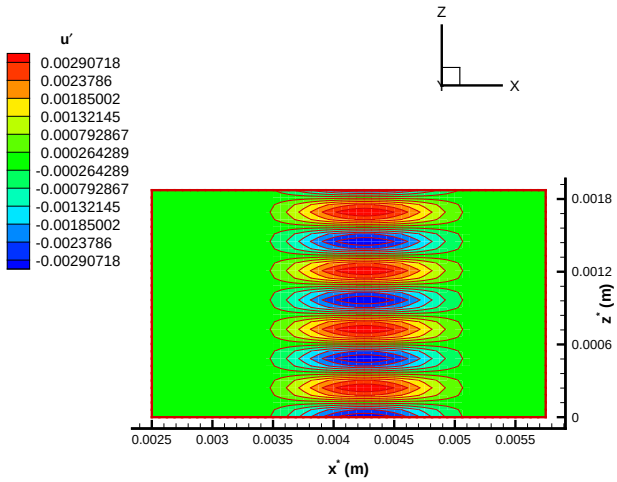

Figure 41: Contours of streamwise velocity perturbation on the plate induced by the roughness element of $\beta^* = 1.3 \times 10^4$ m^{-1}.

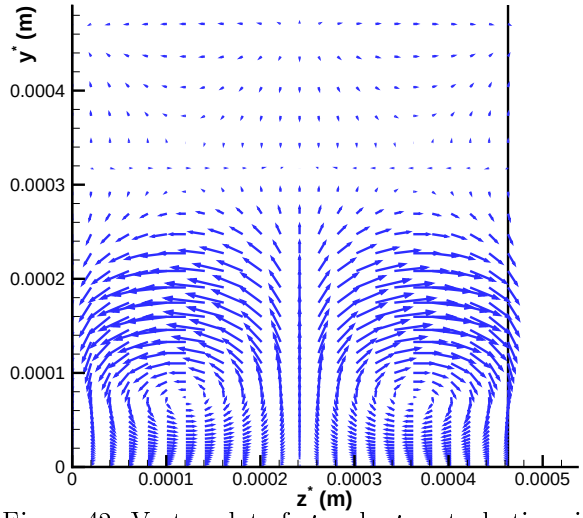

Figure 42: Vector plot of $v\prime$ and $w\prime$ perturbations in the (y, z) plane at a location of $x^* = 5.4375$ mm.

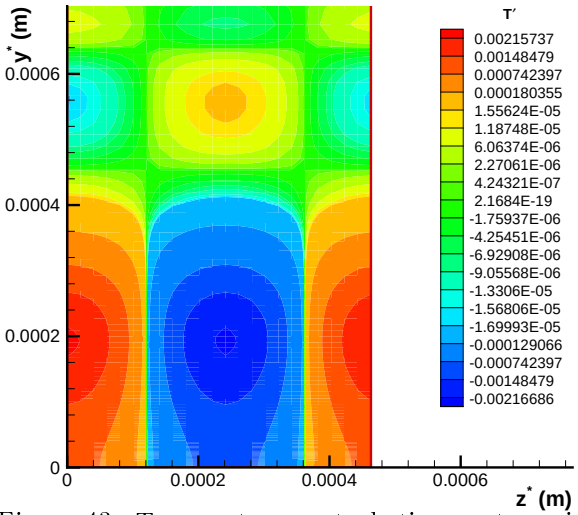

Figure 43: Temperature perturbation contours in the (y, z) plane at a location of $x^* = 5.4375$ mm.

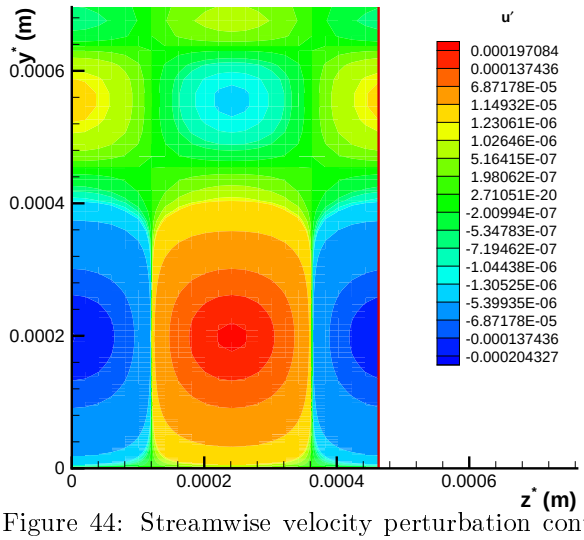

Figure 44: Streamwise velocity perturbation contours in the (y, z) plane at a location of $x^* = 5.4375$ mm.

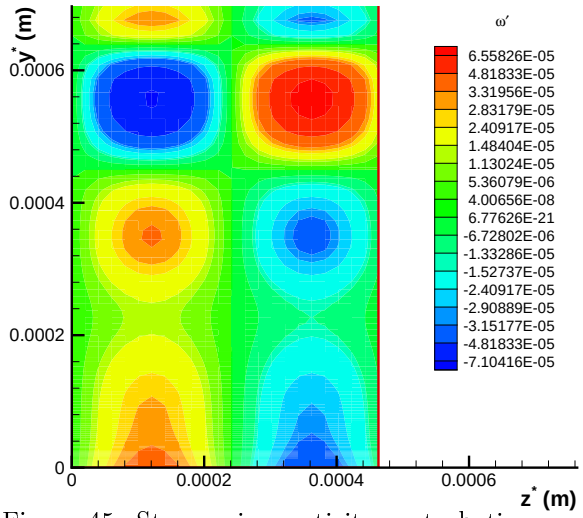

Figure 45: Streamwise vorticity perturbation contours in the (y, z) plane at a location of $x^* = 5.4375$ mm.

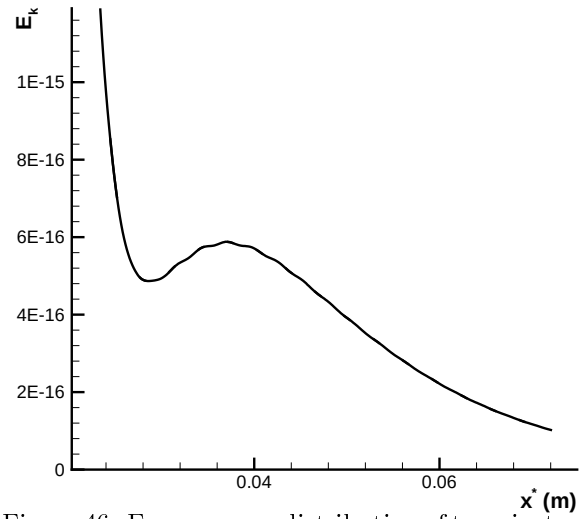

Figure 46: Energy norm distribution of transient growth along the adiabatic flat plate.

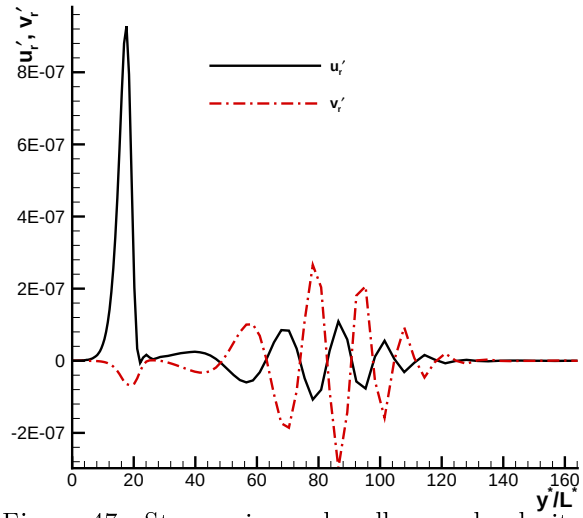

Figure 47: Streamwise and wall-normal velocity perturbations in wall-normal direction at the location of $x^* = 0.040$ m.

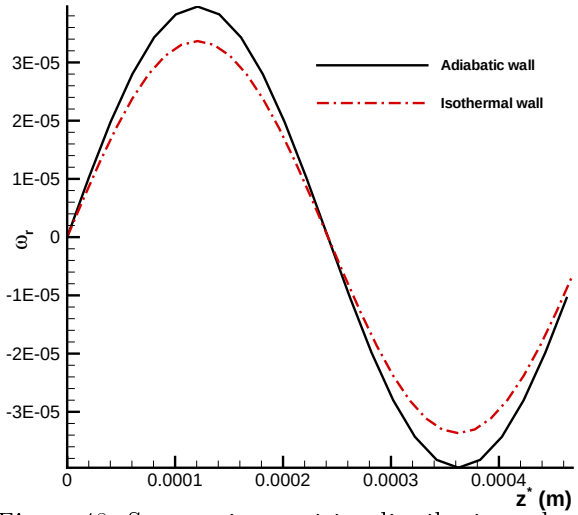

Figure 48: Streamwise vorticity distributions along the adiabatic and isothermal flat plates at $x^* = 5.4375$ mm.

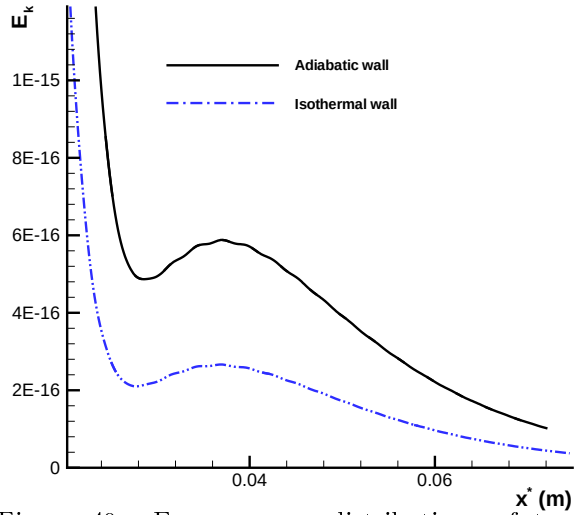

Figure 49: Energy norm distributions of transient growth along the adiabatic and isothermal flat plates.